

The SOFIA Massive (SOMA) Radio Survey. III. Radio Emission from Intermediate-Mass Protostars

FRANCISCO SEQUEIRA-MURILLO ¹, VIVIANA ROSERO ^{2,3}, JOSHUA MARVIL ⁴, JONATHAN C. TAN ^{5,6},
RUBEN FEDRIANI ^{7,5}, YICHEN ZHANG ^{8,6}, PRASANTA GORAI ^{9,10}, JAMES M. DE BUIZER ¹¹ AND
MARIA T. BELTRÁN ¹²

¹*Department of Astronomy, University of Wisconsin-Madison, 475 N. Charter St., Madison, WI 53703, USA*

²*Cahill Center for Astronomy and Astrophysics, MC 249-17, California Institute of Technology, Pasadena, CA 91125, USA*

³*Space Science Institute, 4750 Walnut Street, Suite 205, Boulder, CO 80301, USA*

⁴*National Radio Astronomy Observatory, 1003 Lópezville Rd., Socorro, NM 87801, USA*

⁵*Department of Space, Earth & Environment, Chalmers University of Technology, 412 93 Gothenburg, Sweden*

⁶*Department of Astronomy, University of Virginia, Charlottesville, Virginia 22904, USA*

⁷*Instituto de Astrofísica de Andalucía, CSIC, Glorieta de la Astronomía s/n, 18008 Granada, Spain*

⁸*State Key Laboratory of Dark Matter Physics, School of Physics and Astronomy, Shanghai Jiao Tong University, Shanghai 200240, People's Republic of China*

⁹*Roseland Centre for Solar Physics, University of Oslo, PO Box 1029 Blindern, 0315, Oslo, Norway*

¹⁰*Institute of Theoretical Astrophysics, University of Oslo, PO Box 1029 Blindern, 0315, Oslo, Norway*

¹¹*Carl Sagan Center for Research, SETI Institute, Mountain View, CA, USA*

¹²*INAF-Osservatorio Astrofisico di Arcetri, Largo E. Fermi 5, I-50125 Firenze, Italy*

ABSTRACT

We present results from Very Large Array (VLA) radio continuum observations of twelve intermediate-mass (IM) protostars, as part of the *SOFIA* Massive Star Formation Survey. Using these observations, we studied their morphology, multiplicity and radio spectral energy distributions (SEDs). Across our target regions, we resolve multiple compact sources and report eight new detections, four of which are entirely new and four that have counterparts at other wavelengths, but are detected here for the first time at radio frequencies. Based on radio morphologies and spectral indices, we assess the nature of the detected sources, highlighting seven that display jet-like structures and spectral indices consistent with ionized jets. Combining our results with the SOMA Radio I and II results, we expand the overall sample to 29 protostars, covering a bolometric luminosity range from $L_{\text{bol}} \sim 10^2$ to $10^6 L_{\odot}$. These sources help define a potential evolutionary sequence in the radio versus bolometric luminosity diagram. IM protostars have radio luminosities that are lower than expected from a simple power law extrapolation from low-mass protostars. However, this result is consistent with theoretical expectations from protostellar evolution models, which show low levels of photoionization and reduced shock ionization emission due to expanded stellar radii during this phase. Overall our expanded SOMA Radio sample provides new constraints on theoretical models of massive protostellar evolution, especially the connection to ionized gas structures.

Keywords: Interstellar medium (847) — Radio jets (1347) — Jet outflows (1607) — Stellar astronomy (1583) — Star formation (1569) — Interferometers (805)

1. INTRODUCTION

Intermediate-mass (IM) protostars are classified as those with masses in the range $2 < m_*/M_{\odot} < 8$, i.e., linking the low- and high-mass regimes. IM stars produce more UV photons and are thought to form in more densely clustered environments, compared to the low-

mass protostars (e.g., M. T. Beltrán 2015). These IM star-forming regions are generally closer and less extinguished than massive star-forming regions, making them easier to study.

High-sensitivity centimeter continuum observations provide valuable insights into the earliest and most obscured stages of intermediate- and high-mass star formation. In particular, radio continuum emission plays a crucial role in constraining the ionizing luminosity

of protostars and probing their surrounding environments. V. Rosero et al. (2016, 2019b) showed that many centimeter continuum sources exhibit morphologies and properties characteristic of ionized jets, consistent with the free-free emission models of massive protostars developed by K. E. I. Tanaka et al. (2016). These results highlight the importance of radio continuum observations for testing theoretical models and refining our understanding of the evolutionary sequence of massive star formation.

The SOFIA Massive (SOMA) Star Formation Survey (PI: J. Tan) aims to characterize a sample of ≥ 50 high and intermediate-mass protostars over a range of evolutionary stages, environments, and core masses, using SOFIA-FORCAST $\sim 10\text{--}40\ \mu\text{m}$ data. In Paper I of the survey (J. M. De Buizer et al. 2017) (hereafter SOMA I), the first eight sources were presented, consisting primarily of massive protostars. In Paper II (M. Liu et al. 2019) (hereafter SOMA II), seven high-luminosity sources were presented, which are among the most massive protostars in the survey. In Paper III (M. Liu et al. 2020) (hereafter SOMA III), 14 intermediate-mass sources were presented. In Paper IV (R. Fedriani et al. 2023) (hereafter SOMA IV), 11 isolated sources, based on the $37\ \mu\text{m}$ imaging, were presented. In Paper V (Z. Telkamp et al. 2025) (hereafter SOMA V), seven regions of relatively clustered massive star formation were studied.

Fitting infrared-only radiative transfer (RT) models of massive protostars (e.g., Y. Zhang & J. C. Tan 2018, hereafter ZT18) typically leads to significant degeneracies in key parameters. However, incorporating centimeter continuum data, along with models for free-free emission such as the K. E. I. Tanaka et al. (2016, hereafter TTZ16) models, is expected to help break these degeneracies and thus provide tighter constraints on massive protostellar properties.

This study is the third in a series of centimeter-continuum follow-ups to the SOMA papers. V. Rosero et al. (2019a, hereafter SOMA Radio I) presented and analyzed the first eight sources from SOMA I. Subsequently, F. Sequeira-Murillo et al. (2025, hereafter SOMA Radio II) presented and analyzed nine sources from SOMA II, including two IM protostars G305.20+0.21 A and IRAS 16562–3959 N from SOMA III. Here, we present high-sensitivity Karl G. Jansky Very Large Array (VLA) observations at 1.3 and 6 cm for seven regions containing a total of 12 sources, all of which were analyzed in SOMA III.

Our approach follows the general methodology described in SOMA Radio I and SOMA Radio II to analyze the data and construct the radio spectral energy

distributions (SEDs). This includes reducing the centimeter-continuum observations, measuring flux densities from the images, and analyzing the morphology and multiplicity of each source. These steps ensure that all protostars are analyzed in a uniform and systematic manner. In addition, we present an analysis of the source properties across the SOMA sample, which comprises 29 sources studied in SOMA I, SOMA II, and SOMA III, as well as in their corresponding centimeter-continuum follow-ups (SOMA Radio I, SOMA Radio II, and this work).

Building on the methods outlined in SOMA Radio II, we incorporate the updated SED fitting methods from SOMA V, which introduced several improvements to the general SOMA analysis framework. Accordingly, we adopt the aperture sizes, as well as the infrared data and results (bolometric luminosities, fluxes, and models), from SOMA V in place of those from SOMA III.

Our paper is organized as follows: methodology and information regarding the observations are presented in §2. The observational results for each source are presented in §3, while the analysis and discussion of the sample are presented in §4. The summary and conclusions are presented in §5.

2. METHODS

The SOMA Star Formation Survey sample was constructed from SOFIA-FORCAST observations (i.e., from ~ 10 to $40\ \mu\text{m}$). The sample analyzed in this paper is presented in SOMA III, except for sources G305.20+0.21 A and IRAS 16562–3959 N that were presented in SOMA Radio II. Thus, a total of twelve protostars in seven target regions will be analyzed: S235, IRAS 22198+6336, NGC 2071, Cepheus E, L1206 (A and B), IRAS 22172+5549 (MIR1, MIR2, and MIR3), and IRAS 21391+5802 (BIMA2, BIMA3, and MIR48).

The data analyzed in this study are summarized in Table 1. The first column presents the region names, while columns 2, 3, and 4 provide the band frequency, R.A., and Decl., respectively. Synthesized beam size and position angle (PA), along with the rms of the resulting images, are detailed in columns 5 and 6. The distance to every region, as adopted by SOMA III, as well as the isotropic bolometric luminosities and the bolometric luminosities evaluated by SOMA V, are shown in columns 7, 8, and 9, respectively. Furthermore, Table 2 provides a list of phase calibrators utilized in the observations at 6 and 1.3 cm.

Table 1. SOMA Sources: Radio Continuum Data.

Region	Frequency Band	R.A	Decl.	Beam Size	rms	D ^a	$L_{\text{bol,iso}}$ ^b	L_{bol} ^b
	(GHz)	(J2000)	(J2000)	(" x ", degree)	($\mu\text{Jy beam}^{-1}$)	(kpc)	(L_{\odot})	(L_{\odot})
S235	4.0 – 8.0	05 40 52.40	+35 41 30.0	0.30×0.28 , +80.8	4.9	1.8	$2.2^{+2.3}_{-1.1} \times 10^3$	$2.6^{+6.9}_{-1.9} \times 10^4$
	18.0 – 26.0	0.39×0.24 , +77.1	9.7
IRAS 22198+6336	4.0 – 8.0	22 21 26.68	+63 51 38.2	0.59×0.28 , –71.6	4.2	0.764	$3.9^{+17.8}_{-3.2} \times 10^2$	$8.0^{+20.2}_{-5.7} \times 10^2$
	18.0 – 26.0	0.42×0.24 , –87.6	8.9
NGC 2071	4.0 – 8.0	05 47 04.74	+00 21 42.9	0.29×0.27 , –59.6	7.6	0.43	$3.6^{+9.1}_{-2.6} \times 10^2$	$6.9^{+12.0}_{-4.4} \times 10^2$
	18.0 – 26.0	0.31×0.25 , +16.2	13.7
Cepheus E	4.0 – 8.0	23 03 12.8	+61 42 26.0	0.33×0.28 , +8.05	3.5	0.73	$3.3^{+10.1}_{-2.5} \times 10^2$	$7.4^{+14.3}_{-4.9} \times 10^2$
	18.0 – 26.0	0.63×0.30 , –73.9	9.7
L1206	4.0 – 8.0	22 28 51.41	+64 13 41.1	0.39×0.37 , +48.1	4.5	0.776	$1.7^{+0.7}_{-0.5} \times 10^3$	$3.7^{+3.3}_{-1.7} \times 10^3$
	18.0 – 26.0	0.55×0.30 , –85.7	8.2
IRAS 22172+5549	4.0 – 8.0	22 19 09.48	+56 05 00.4	0.41×0.32 , –75.6	6.6	2.4	$1.5^{+1.9}_{-0.8} \times 10^3$	$6.2^{+26.1}_{-5.0} \times 10^4$
	18.0 – 26.0	0.46×0.24 , –78.2	8.7
IRAS 21391+5802	4.0 – 8.0	21 40 41.90	+58 16 12.3	0.66×0.28 , –67.1	4.0	0.75	$9.9^{+9.8}_{-4.9} \times 10^1$	$5.6^{+7.0}_{-3.1} \times 10^2$
	18.0 – 26.0	0.41×0.24 , –84.7	9.1

NOTE— Units of R.A. are hours, minutes, and seconds. Units of decl. are degrees, arcminutes, and arcseconds.

^a References cited in [SOMA III](#), except for NGC 2071, where we use the values from [J. J. Tobin et al. \(2020\)](#) with Gaia observations.

^b Average and dispersion of the bolometric luminosities of the good models from [SOMA V](#), these values and other intrinsic properties are reported in Table C1.

Table 2. VLA Calibrators.

Calibrator	Astrometry Precision ^a	Source Calibrated	Band
J0555+3948	A	S235	C, K
J2230+6946	A	IRAS 22198+6336	C
J2148+6107	C	IRAS 22198+6336	K
J0541-0541	A	NGC 2071	C, K
J2230+6946	A	Cepheus E	C
J2148+6107	C	Cepheus E	K
J2230+6946	A	L1206	C
J2148+6107	C	L1206	K
J2202+4216	A	IRAS 22172+5549	C
J2148+6107	C	IRAS 22172+5549	K
J2022+6136	B	IRAS 21391+5802	C
J2148+6107	C	IRAS 21391+5802	K

NOTE—

^a Astrometric precisions of A, B and C correspond to positional accuracies of <0.002 arcsec, 0.002–0.01 arcsec and 0.01–0.15 arcsec, respectively.

2.1. VLA Data

2.1.1. The 6 cm Data

The 6 cm (C-Band) observations were made in the A configuration, providing angular resolutions of $\sim 0''.3$ – $0''.6$. The data for regions S235, IRAS 22198+6336, NGC 2071, Cepheus E, and IRAS 21391+5802, consist of two ~ 2 GHz wide basebands (3-bit samplers) centered at 5.03 and 6.98 GHz. The data were recorded

in 30 unique spectral windows (SPWs), each comprised of 64 channels and each channel being 2 MHz wide, resulting in a total bandwidth of 3842 MHz (before “flagging”). Source 3C48 was used as flux density and bandpass calibrator for regions S235, NGC 2071, and Cepheus E, and 3C286 was used as flux density and bandpass calibrator for regions IRAS 22198+6336 and IRAS 21391+5802. Meanwhile, the data for regions L1206 and IRAS 22172+5549, consist of two 1 GHz wide basebands (8-bit samplers) centered at 5.3 and 6.3 GHz. The data were recorded in 16 unique SPWs, each comprised of 64 channels and each channel being 2 MHz wide, resulting in a total bandwidth of 2048 MHz (before “flagging”). Source 3C48 was used as a flux density and bandpass calibrator.

Table 3 shows approximations of the observation times for each source at both 6 and 1.3 cm bands. All the observations were made by alternating between the target source and the phase calibrator. Column 3 shows the project code of the observations, columns 4 and 5 show these alternating times, and column 6 shows the total integration time for each observation.

Data reduction was carried out in a manner similar to the VLA observations from the [SOMA Radio II](#). We used calibrated data from the 41154 (Pipeline-CASA51-P2-B) version of the VLA Calibration Pipeline¹³ for

¹³ science.nrao.edu/facilities/vla/data-processing/pipeline

regions IRAS 22198+6336, Cepheus E, and IRAS 21391+5802. For region NGC 2071, we used the VLA Calibration Pipeline version 2021.2.0.128, and for region S235, we used the VLA Calibration Pipeline version 42536 (Pipeline-CASA54-P3-B-SRDP). The differences in the data reduction pipelines arise from the year of the observations and the version of the VLA Calibration Pipeline available at that time (see column 3 in Table 3). The images were made in CASA (CASA Team et al. 2022) using the *tclean* task and a Briggs *Robust* = 0.5 weighting (D. S. Briggs 1995).

For regions S235, IRAS 22198+6336, NGC 2071, Cepheus E, and IRAS 21391+5802, we made two images, each of a ~ 2 GHz baseband composed of 15 SPWs, and also a combined image using data from both basebands with a total of 30 SPWs. For regions L1206 and IRAS 22172+5549, we made two images, each of a ~ 1 GHz baseband composed of 8 SPWs, and also a combined image using data from both basebands with a total of 16 SPWs. All maps were primary beam-corrected. Columns 5 and 6 of Table 1 show the synthesized beam (size and position angle) and the rms of the combined images.

2.1.2. The 1.3 cm Data

The 1.3 cm (K-Band) observations were made in the B configuration, providing angular resolutions of $\sim 0''.3$ - $0''.6$. The data consist of two ~ 4 GHz wide basebands (3-bit samplers) centered at 20.4 and 24.4 GHz, except for regions S235 and NGC 2071, centered at 20.5 and 24.5 GHz. The data were recorded in 60 (62 for source L1206) unique SPWs, comprised of 64 channels and each channel being 2 MHz wide, resulting in a total bandwidth of 7680 MHz (7936 MHz for source L1206), before “flagging”. Source 3C286 was used as a flux density and bandpass calibrator for all the regions except for NGC 2071, where source 3C48 was used as a flux density and bandpass calibrator. Additional information about the observations can be found in Table 3.

The data reduction was done in the same manner as that for the C-Band observations and using the VLA Calibration Pipeline version 2021.2.0.128 for regions S235 and NGC 2071, and the VLA Calibration Pipeline version 42270 (Pipeline-CASA54-P2-B) for the other regions. The images were made using the *tclean* task and a Briggs *Robust* = 0.5 weighting. We made two images, each of a ~ 4 GHz baseband composed of 30 SPWs, and also a combined image using data from both basebands with a total of 60 SPWs for all sources except L1206, that have a total of 62 SPWs. All maps were primary beam-corrected. Columns 5 and 6 of Table 1 show the

Table 3. Observations times for each source in minutes.

Source	Band	Project ^a	Target	Phase	Total
		Code	Source ^b	Calibrator ^b	Integration
			(min)	(min)	(min)
S235	C	19A-216	9.3	0.5	37.2
	K	21B-229	2.4	0.6	21.8
IRAS 22198+6336	C	18A-294	8.4	0.5	42.1
	K	19A-216	1.3	0.5	23.3
NGC 2071	C	22A-125	7.9	0.5	39.5
	K	21B-229	2.3	0.5	20.9
Cepheus E	C	18A-294	8.2	0.4	40.9
	K	19A-216	2.2	0.4	19.6
L1206	C	12B-140 ^c	6.4	0.6	31.8
	K	19A-216	1.2	0.5	21.8
IRAS 22172+5549	C	12B-140 ^c	6.4	0.6	31.8
	K	19A-216	1.3	0.6	22.6
IRAS 21391+5802	C	18A-294	8.2	0.4	40.8
	K	19A-216	1.4	0.6	24.4

NOTE—

^a Project code from the VLA observations. The first two numbers in the project code denotes the year in which the observations were made, e.g., 19A corresponds to observations taken in 2019.

^b Alternating time from source to calibrator.

^c Observations with project code 12B-140 were Jansky VLA public archival data (PI: M. Hoare), the rest of the observations were our own (PI: V. Rosero).

synthesized beam (size and position angle) and the rms of the combined images.

3. RESULTS

We follow the methodology described in **SOMA Radio I** and **SOMA Radio II** (see Section 4 of **SOMA Radio I** for further details). In brief, a radio detection is defined when the peak intensity I_ν is ≥ 5 times the image rms (σ) in either of the baseband-combined images at a given band (i.e., C band or K band). For non-detections in one of the combined images, we report a 3σ upper limit for the flux density at the corresponding frequency. Figure 1 shows VLA contour plots of the combined images at C band (6 cm; red) and K band (1.3 cm; cyan) for all the radio sources, overlaid on SOFIA/FORCAST $37\ \mu\text{m}$ images. The infrared data from M. Liu et al. (2020) (including SOFIA, *Herschel*, and *Spitzer* observations) and the VLA data presented here have astrometric accuracies better than $1''.5$ and $0''.1$ (see Table 2), respectively.

The spatial scales and the procedures used to measure flux densities and their uncertainties follow those in **SOMA Radio I** and **SOMA Radio II**. For the *SOMA* and *Intermediate* scales (see below for definitions), we used the CASA task *imstat* with the aperture sizes listed in Table 5. For the *Inner* scale, flux densities were obtained with the CASA task *imfit*. A detailed discussion of the uncertainty calculations is provided in Section 4 of **SOMA Radio I**.

Table 4 lists the radio parameters for each of the 12 protostars studied in this paper. These parameters are

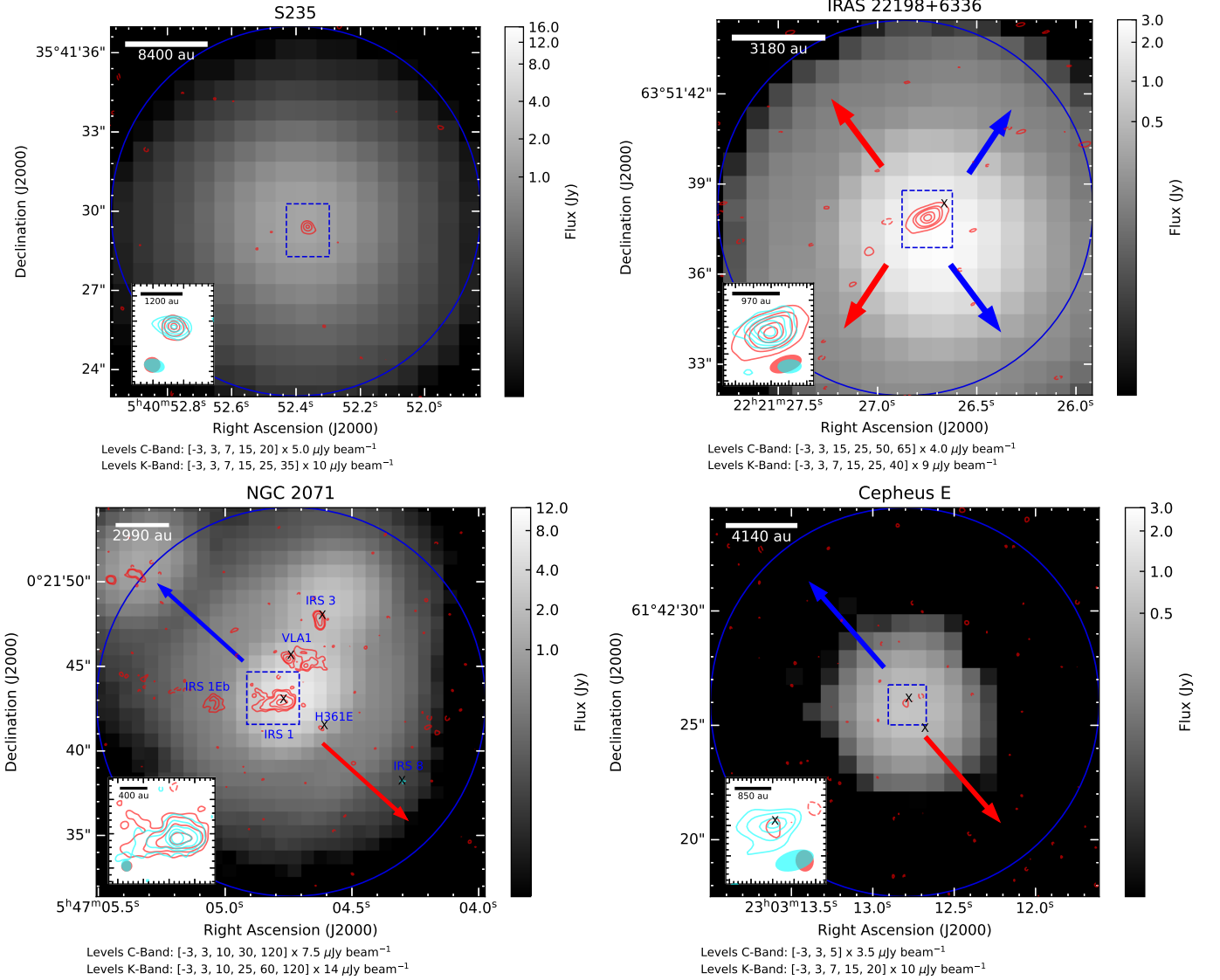


Figure 1. Images are SOFIA-FORCAST 37 μm with VLA contours – red: C-band (6 cm); cyan: K-band (1.3 cm) – of the combined radio maps overlaid. The blue dashed squares correspond to the area and the location of the inset image showing a zoom-in of the central region, and the synthesized beams are shown in the lower corners of these insets. The cyan crosses in NGC 2071 denotes the position of detections only at K-band (cyan contours). The black \times denotes the position of the mm core on the regions with millimeter observations, references as follows: IRAS 22198+6336: [Á. Sánchez-Monge et al. \(2010\)](#), NGC 2071: [Y. Cheng et al. \(2022\)](#), Cepheus E: [J. Ospina-Zamudio et al. \(2018\)](#), L1206 A: [M. T. Beltrán et al. \(2006\)](#), IRAS 21391+5802 BIMA2 and BIMA3: [R. Neri et al. \(2007\)](#). The blue circles are the SOMA apertures used by SOMA V and reported in Table C1. The blue and red arrows represent the direction of a molecular outflow detected toward the region, only for regions with know association with molecular outflows (references are given in section 3.1). A scale bar in units of au is shown in the upper left of the figures.

measured at three spatial scales, defined as follows. The *SOMA* scale corresponds to the aperture radius used in SOMA V to measure the infrared fluxes. The *Intermediate* scale is based on the morphology of the radio source, specifically whether the detections exhibit jet-like structures. In the sample analyzed here, only NGC 2071 display such morphology. The *Inner* scale corresponds to

the size of the central radio emission that is most likely associated with the driving protostar.

Columns 1 and 2 of Table 4 list the region and spatial scale. For each scale, Columns 3 and 4 give the R.A. and Decl. coordinates. For the *SOMA* scale, these values correspond to the SOFIA/FORCAST pointing centers reported in [M. Liu et al. \(2020, Table 1\)](#). For the *Intermediate* scale, they represent the midpoint of

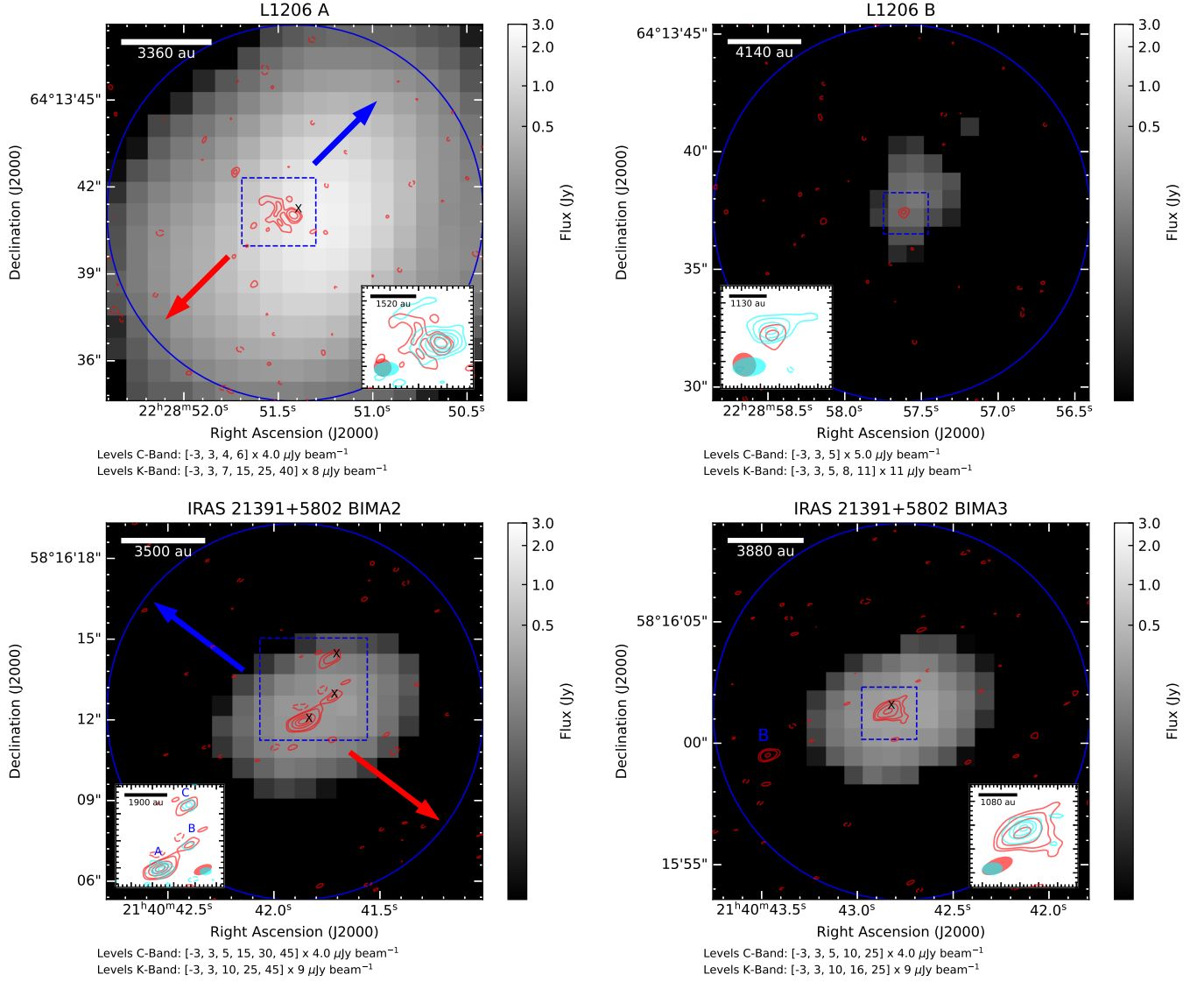


Figure 1. (Continued)

the jet-like detection, while for the *Inner* scale, they correspond to the peak intensity position of the central detected object. The subsequent columns list the flux densities (S_ν) at various frequencies, with the cor-

responding uncertainties given in parentheses. The final column in Table 4 reports the spectral indices and their uncertainties for each scale (see Section 3.2).

Table 4. Parameters from Radio Continuum.

Region	Scale	R.A	Decl.	$S_{5.0\text{ GHz}}$	$S_{7.0\text{ GHz}}$	$S_{20.6\text{ GHz}}$	$S_{24.5\text{ GHz}}$	Spectral
		(J2000)	(J2000)	(mJy)	(mJy)	(mJy)	(mJy)	Index
S235	SOMA	05:40:52.40	+35.41.30.00	1.33(0.24)	0.31(0.28)	0.46(0.42)	<1.76	<-0.3
	<i>Intermediate</i>
	<i>Inner</i>	05:40:52.37	+35.41.29.39	0.11(0.01)	0.12(0.02)	0.32(0.03)	0.42(0.05)	0.9(0.1)

Table 4 continued

Table 4 (continued)

Region	Scale	R.A.	Decl.	$S_{5.0\text{ GHz}}$	$S_{7.0\text{ GHz}}$	$S_{20.6\text{ GHz}}$	$S_{24.5\text{ GHz}}$	Spectral
		(J2000)	(J2000)	(mJy)	(mJy)	(mJy)	(mJy)	Index
IRAS 22198+6336	SOMA	22:21:26.68	+63.51:38.20	0.47(0.12)	0.45(0.20)	0.68(0.33)	0.86(0.45)	0.3(0.5)
	<i>Intermediate</i>
	<i>Inner</i>	22:21:26.75	+63.51:37.92	0.24(0.09)	0.53(0.06)	0.78(0.09)	0.80(0.13)	0.5(0.1)
NGC 2071 ^a	SOMA	05:47:04.74	+00.21:42.96	8.21(1.15)	7.01(0.98)	10.47(1.41)	10.87(1.90)	0.3(0.1)
	<i>Intermediate</i>	05:47:04.70	+00.21:45.41	1.76(0.20)	1.29(0.15)	2.39(0.26)	2.65(0.31)	0.4(0.1)
	<i>Inner</i>	05:47:04.79	+00.21:42.96	4.88(0.49)	4.51(0.45)	6.11(0.61)	6.81(0.68)	0.2(0.1)
Cepheus E	SOMA	23:03:12.80	+61.42:26.00	0.02(0.17)	<0.80	0.03(0.39)	<1.48	<0.9
	<i>Intermediate</i>
	<i>Inner</i>	23:03:12.80	+61.42:26.04	<0.01	<0.01	0.19(0.03)	0.27(0.04)	>2.1
L1206 A	SOMA	22:28:51.41	+64.13:41.10	0.04(0.18)	0.23(0.21)	1.36(0.29)	1.60(0.41)	1.7(1.2)
	<i>Intermediate</i>
	<i>Inner</i>	22:28:51.43	+64.13:41.00	0.15(0.03)	0.08(0.03)	0.43(0.05)	0.24(0.09)	0.9(0.2)
L1206 B	SOMA	22:28:51.41	+64.13:41.10	0.05(0.21)	<0.80	0.56(0.41)	0.22(0.64)	>1.2
	<i>Intermediate</i>
	<i>Inner</i>	22:28:51.43	+64.13:41.00	0.05(0.01)	0.03(0.01)	0.16(0.02)	0.17(0.04)	1.1(0.1)
IRAS 22172+5549 MIR1	SOMA	22:19:08.33	+56.05:10.52	0.17(0.31)	<1.23	<1.25	<1.63	<0.7
	<i>Intermediate</i>
	<i>Inner</i>	<0.03	<0.03	<0.03	<0.04	<0.2
IRAS 22172+5549 MIR2	SOMA	22:19:09.48	+56.05:00.37	<0.44	0.38(0.21)	<0.68	<0.90	<0.5
	<i>Intermediate</i>
	<i>Inner</i>	<0.03	<0.03	<0.04	<0.04	<0.3
IRAS 22172+5549 MIR3	SOMA	22:19:09.43	+56.04:45.58	0.05(0.31)	0.05(0.44)	0.03(0.50)	0.09(0.59)	0.1(2.7)
	<i>Intermediate</i>
	<i>Inner</i>	<0.03	<0.03	<0.04	<0.04	<0.3
IRAS 21391+5802 BIMA2 ^b	SOMA	21:40:41.90	+58.16:12.30	0.27(0.13)	0.36(0.18)	0.52(0.41)	0.73(0.51)	0.5(0.8)
	<i>Intermediate</i>
	<i>Inner</i>	21:40:41.86	+58.16:11.93	0.23(0.03)	0.26(0.03)	0.64(0.07)	0.58(0.07)	0.7(0.1)
IRAS 21391+5802 BIMA3	SOMA	21:40:42.77	+58.16:01.28	0.14(0.16)	0.22(0.20)	0.26(0.44)	0.42(0.57)	0.5(1.7)
	<i>Intermediate</i>
	<i>Inner</i>	21:40:42.85	+58.16:01.46	0.01(0.02)	0.18(0.03)	0.30(0.04)	0.20(0.07)	0.9(0.2)
IRAS 21391+5802 MIR48	SOMA	21:40:41.43	+58.16:38.09	0.07(0.16)	<0.61	<1.43	<1.93	<1.3
	<i>Intermediate</i>
	<i>Inner</i>	<0.02	<0.02	<0.04	<0.04	<0.6

NOTE— The Intermediate scale corresponds to the extent of the radio jet, see Table 5 for scale definitions. Units of R.A. are hours, minutes, and seconds. Units of decl. are degrees, arcminutes, and arcseconds.

^a Inner scale detection corresponds to the location of source IRS1 (more details in section 3.1.3).

^b Inner scale detection corresponds to the location of source VLA 2 (more details in section 3.1.7).

3.1. Morphology and Multiplicity

All target regions presented in this paper have been observed in the centimeter continuum; we describe their morphology as “compact” if the detection shows no structure on the scale of a few synthesized beams, or “extended” otherwise. Next, we describe the centimeter wavelength detections toward each target. For a de-

tailed background on each of these regions, see [SOMA II](#); [SOMA III](#).

3.1.1. S235

S235 A and S235 B are regions located at a distance of 1.8 kpc ([M. Nakano & S. Yoshida 1986](#); [L. K. Dewangan et al. 2016](#)) and form part of the extended star-forming region S235 within the giant molecular cloud G174+2.5 in the Perseus spiral arm ([M. H. Heyer et al.](#)

Table 5. SOMA, *Intermediate* and *Inner* Scales.

Region	SOMA	<i>Intermediate</i>	Inner
	R (")	w (") \times h (")	a (") \times b (")
S235	7.0	...	0.35×0.22^a
IRAS 22198+6336	6.25	...	0.55×0.38^a
NGC 2071	11.5	2.83×1.65	1.05×0.61^b
Cepheus E	7.5	...	0.70×0.37^b
L1206 A	6.5	...	0.63×0.39^a
L1206 B	8.0	...	0.62×0.31^a
IRAS 22172+5549 MIR1	8.0
IRAS 22172+5549 MIR2	3.8
IRAS 22172+5549 MIR3	7.75
IRAS 21391+5802 BIMA2	7.0	...	0.32×0.25^b
IRAS 21391+5802 BIMA3	7.75	...	0.53×0.33^a
IRAS 21391+5802 MIR48	7.75

NOTE— The reported values correspond to a circle of radius R for the SOMA scale and a box of height h and width w for the *Intermediate* scale. In some cases the inner scale between the C and K images are different so we report the larger area that we consider any source of emission within the inner region, we also have two different types of regions:

^a Scale corresponds to image component (convolved with beam) size from the task imfit, of major axis a and minor axis b .

^b Scale corresponds to an ellipse of major axis a and minor axis b .

1996). For our analysis, we focus on S235 B, classified by P. A. Boley et al. (2009) as an early-type (B1 V) Herbig Be star based on low- and medium-resolution spectra, whose spectral type, emission lines, nebulosity, and environment meet the criteria for HBe stars defined by G. H. Herbig (1960).

In our observations, we detect a single compact source at both 6 cm and 1.3 cm. This detection is consistent with the results of M. Felli et al. (2006), who also observed the source at these wavelengths, naming it VLA-2 and reporting a flux density of 0.47 mJy with a resolution of 1'' at 1.3 cm. At 6 cm, they reported an upper limit of 0.27 mJy with a resolution of 3''. The flux density measured in our 6 cm observations is within this upper limit.

M. Felli et al. (2006) reported an observed spectral index smaller than 0.6 for VLA-2. In our observations, we report an estimated value of the spectral index of $\alpha \sim 0.9$. This result may indicate that the source is a point source associated with thermal emission. This interpretation is consistent with the observed morphology, which appears compact and not elongated in any direction.

Our results, showing a compact morphology and a spectral index consistent with thermal emission, reinforce the Herbig Be star classification proposed by P. A.

Boley et al. (2009) and support the conclusion regarding the nature of S235 B.

3.1.2. IRAS 22198+6336

IRAS 22198+6336 is an intermediate-mass protostar located at 764 ± 27 pc (T. Hirota et al. 2008). Due to the presence of a strong and compact submillimeter dust condensation (T. Jenness et al. 1995) and no near-infrared observation, Á. Sánchez-Monge et al. (2008) proposed that IRAS 22198+6336 is a deeply embedded intermediate-mass YSO, classified as an early-type B protostar in an evolutionary stage similar to Class 0 source in the low-mass regime. CO(1-0) and CO(2-1) maps from Á. Sánchez-Monge et al. (2010) reveal an outflow with a quadrupolar morphology clearly centered on the position of the dust condensation.

In our observations, we detected a single source at both 6 cm and 1.3 cm, slightly elongated along the NW–SE direction. This source, previously reported as VLA 2 by Á. Sánchez-Monge et al. (2008), was observed at 3.6, 1.3, and 0.7 cm with angular resolutions of $\sim 9.6''$, $\sim 3.2''$, and $\sim 1.7''$, respectively. Their spectral index of ~ 0.5 agrees with our results and is typical of ionized jets associated with YSOs (e.g., S. P. Reynolds 1986; G. Anglada et al. 1998; K. E. I. Tanaka et al. 2016). Furthermore, the source’s elongated morphology and likely alignment with a larger-scale NW-SE molecular outflow support this interpretation.

3.1.3. NGC 2071

NGC 2071 is an intermediate-mass star-forming region in the L1630 molecular cloud of Orion B, located at a distance of 430 pc (J. J. Tobin et al. 2020). A bipolar molecular outflow has been observed toward NGC 2071, oriented in the northeast–southwest direction, extending $\sim 15'$ in length and reaching velocities of ~ 120 km s $^{-1}$. This outflow has been studied in CO (J. Bally 1982), HI (J. Bally & A. A. Stark 1983), OH (A. Ruiz et al. 1992), as well as SiO and CH₃OH (G. Garay et al. 2000).

In our observations, we detected 7 sources at both 1.3 and 6 cm, and an additional detection only at 1.3 cm. Several of these sources were previously detected using VLA observations, such as the studies of M. A. Trinidad et al. (2009) at 1.3 cm (K-band) with an angular resolution of $\sim 0.1''$ and a sensitivity of $160 \mu\text{Jy/beam}$, and C. Carrasco-González et al. (2012) at 20 cm (L), 6 cm (C), 3.6 cm (X) and 2 cm (Ku), with resolutions of $\sim 1.44''$, $\sim 0.71''$, $\sim 0.35''$ and $\sim 0.18''$, respectively. In Table 6 we present more information about the multiplicity towards NGC 2071, such as the R.A. and Decl. positions, the estimated spectral index, association with other wavelengths, and whether each source is a new radio detection or not. We present below an individual discussion of each detected source.

Table 6. Multiplicity in NGC 2071.

Detection	R.A (J2000)	Decl. (J2000)	Spectral Index	Association	New Detection
IRS 1	05:47:04.78	+00.21.42.93	0.2 (0.08)	IR, mm	No
IRS 1Eb	05:47:05.04	+00.21.42.82	0.1 (0.5)	...	Yes ^a
VLA 1	05:47:04.75	+00.21.45.43	0.4 (0.11)	X-ray, mm	No
VLA 1-B1	05:47:04.68	+00.21.45.07	0.1 (0.10)	...	Yes ^a
VLA 1-B2	05:47:04.65	+00.21.45.20	0.1 (0.19)	...	Yes ^a
HOPS-361-E-cm	05:47:04.31	+00.21.38.05	<1.1	mm	Yes ^b
IRS 8-cm	05:47:04.62	+00.21.41.32	<0.7	IR, mm	Yes ^b
IRS 3	05:47:04.63	+00.21.47.84	0.4 (0.10)	IR, mm	No

NOTE— Units of R.A. are hours, minutes, and seconds. Units of Decl. are degrees, arcminutes, and arcseconds.

^a These sources have been observed but not detected.

^b These sources have been previously detected at different wavelengths but not in radio continuum.

IRS 1: From our results, we find this source to have an extended morphology elongated in the E–W direction, consistent with previous reports by [M. A. Trinidad et al. \(2009\)](#) and [C. Carrasco-González et al. \(2012\)](#). Using higher-resolution 1.3 cm observations ($\sim 0.1''$, which is ~ 3 times higher than our observations), [M. A. Trinidad et al. \(2009\)](#) resolved the source into three continuum peaks, IRS 1C, IRS 1W, and IRS 1E, and proposed that IRS 1W and IRS 1E are condensations ejected by IRS 1C, the latter being an ionized jet associated with a YSO. All three sources are associated with water masers, consistent with the jet scenario. In addition, [M. A. Trinidad et al. \(2009\)](#) detected an ionized source, IRS 1Wb, located $\sim 1''.8$ southwest of IRS 1C, which is not associated with water masers. Interestingly, we do not detect this source despite our observations being ~ 10 times more sensitive.

Given its complex morphology and spectral index ($\alpha \sim 0.45$) between 20–1.3 cm, [C. Carrasco-González et al. \(2012\)](#) suggested that the emission from IRS1 is arising from the superposition of two jets due to a binary system. Our estimated spectral index for the inner scale of IRS 1 is slightly flatter (see Table 6) than their reported one, but it is still consistent with thermal emission.

IRS 1Eb: We detected this source at both C and K bands, and to the best of our knowledge it has not been previously reported. However, a point source at a close position is visible in Fig. 1 of [C. Carrasco-González et al. \(2012\)](#), which shows 3.6 cm VLA data at comparable resolution, but was not discussed by the authors. Figure 2 shows the VLA 3.6 continuum map from [C. Carrasco-González et al. \(2012\)](#) with VLA contours overlaid from

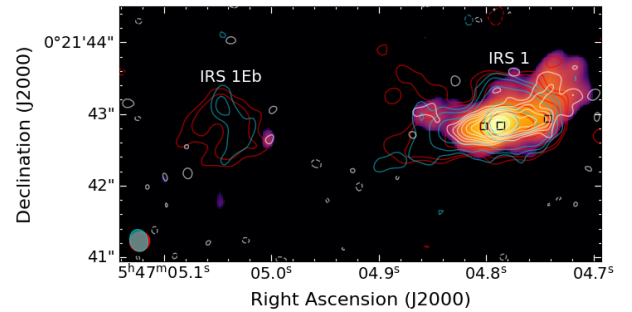


Figure 2. VLA 3.6 continuum map and contours (white) from Fig. 1 in [C. Carrasco-González et al. \(2012\)](#) (see more details on their paper regarding the radio maps), of the radio sources IRS 1 and IRS 1Eb in the NGC 2071 region with VLA contours overlaid (1.3–cyan, 3.6–white, and 6 cm–red). The contour levels are at $[-3, 3, 5, 10, 50, 100] \times 13.7 \mu\text{Jy/beam}$ for 1.3 cm (K-band), at $[-3, 3, 5, 7, 10, 15, 20, 40, 60] \times 30 \mu\text{Jy/beam}$ for 3.6 cm, and at $[-3, 3, 5, 15, 60, 120] \times 7.6 \mu\text{Jy/beam}$ for 6 cm (C-band). The beam sizes of the 1.3 and 6 cm observations are indicated in the lower left-hand corner.

our observations at both C and K band, of sources IRS1 and IRS 1Eb. From this figure we can see the compact source and how it is close to the position of the contours from our observations. This may indicate that the point source from [C. Carrasco-González et al. \(2012\)](#) is related to source IRS 1Eb.

Moreover, no millimeter or infrared counterpart is found in the literature. The source shows two peaks, slightly elongated in the NE–SW direction, and lies $\sim 4''$ east of IRS 1C, roughly aligned with the centimeter emission from IRS 1. Its spectral index of $\alpha \sim 0.1$ is consistent with thermal emission. Given these charac-

teristics, we speculate that IRS 1Eb may trace ejected material from IRS 1C.

IRS 3: In our data, this source appears slightly elongated in the N-S direction, displaying a jet-like morphology and a spectral index consistent with previous studies (J. M. Torrelles et al. 1998; C. Carrasco-González et al. 2012; M. A. Trinidad et al. 2009). M. A. Trinidad et al. (2009) resolved it into three components, IRS 3C, IRS 3N, and IRS 3S. However, we do not resolve these three components at the lower resolution of our data.

Our results are consistent with previous studies that describe this source as an ionized jet. Furthermore, it is thought to be part of a jet-disk system, with the disk-like structure traced by 3 mm continuum emission and water masers distributed along the disk plane (C. Carrasco-González et al. 2012).

Figure 3 shows the VLA 3.6 cm continuum map from C. Carrasco-González et al. (2012) with VLA contours overlaid from our observations at both 6 cm (C-band) and 1.3 cm (K-band), of source IRS 3. C. Carrasco-González et al. (2012) presented several epochs of 3.6 cm continuum maps toward this source between 1998 and 1999 in Fig. 5 of their paper. They interpret the difference in the size of the source due to an ejection of ionized material together with the precession of the jet. We see an increase in the size of the emission from IRS3 when comparing the 1.3 cm and 6 cm contours with the 3.6 cm contours from C. Carrasco-González et al. (2012).

VLA 1: From our observations, we detect a compact source previously reported as VLA 1 by M. A. Trinidad et al. (2009) and C. Carrasco-González et al. (2012). Our estimated spectral index, along with the overall morphology of the system, suggests that this source is likely an ionized jet. Moreover, M. A. Trinidad et al. (2009) and C. Carrasco-González et al. (2012) proposed that VLA 1 is a younger and more deeply embedded YSO compared to other sources in the region, as it is associated with millimeter and X-ray emission, but remains undetected at infrared wavelengths.

VLA 1-B1 and VLA 1-B2: We detect two new point sources at both 1.3 and 6 cm, labeled VLA1-B1 and VLA1-B2, which, to the best of our knowledge, have not been previously reported (see Figure 4). These sources are separated by $\sim 0''.5$ and located $\sim 1''$ and $\sim 1''.5$ southwest of VLA1, respectively. Both are aligned with the centimeter emission from VLA1 and appear slightly extended, with an additional peak north of VLA1-B1. Their estimated spectral indices of ~ 0.1 are consistent with optically thin free-free emission. Neither source appears to be associated with 3mm emission based on Figure 1 of C. Carrasco-González et al. (2012).

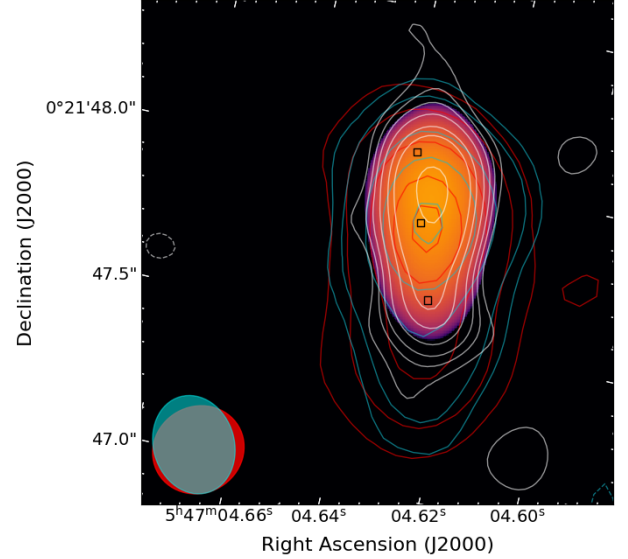


Figure 3. VLA 3.6 cm continuum map and contours (white) from Fig. 1 in C. Carrasco-González et al. (2012) (see more details on their paper regarding the radio maps), of the radio source IRS 3 in the NGC 2071 region with VLA contours overlaid (1.3–cyan, 3.6–white, and 6 cm–red). The contour levels are at $[-3, 3, 5, 10, 50, 100] \times 13.7 \mu\text{Jy/beam}$ for 1.3 cm (K-band), at $[-3, 3, 5, 7, 10, 15, 20, 40, 60] \times 30 \mu\text{Jy/beam}$ for 3.6 cm, and at $[-3, 3, 5, 15, 60, 120] \times 7.6 \mu\text{Jy/beam}$ for 6 cm (C-band). The beam sizes are indicated in the lower left-hand corner.

It is noteworthy that VLA1-B1, the brighter of the two sources, with peak intensities of $380 \mu\text{Jy}$ and $320 \mu\text{Jy}$ at 1.3 and 6 cm, respectively, should have been detectable in previous studies. Based on the reported sensitivities of $40 \mu\text{Jy/beam}$ at 6 cm (C. Carrasco-González et al. 2012) and $70 \mu\text{Jy/beam}$ at 1.3 cm (M. A. Trinidad et al. 2009), VLA1-B1 would correspond to an $\sim 8\sigma$ and $\sim 5\sigma$ detection, respectively. However, it was not detected in those studies, nor was it detected at 3.6 cm (X-band) in C. Carrasco-González et al. (2012), which had a sensitivity of $19 \mu\text{Jy/beam}$.

While the nature of these sources remains uncertain, their spectral indices, alignment with the jet axis, and lack of millimeter counterparts suggest they may be ionized ejecta from VLA 1.

IRS 8-cm and HOPS-361-E-cm: We report two newly detected weak, compact centimeter sources, HOPS-361-E-cm and IRS 8-cm, both identified only at 1.3 cm with 5σ significance. HOPS-361-E-cm shows a marginal 4σ detection at 6 cm (see Figure 5), while IRS 8-cm is undetected at this frequency, with its position marked by an “x” in Figure 1. Both sources are spatially associated with 1.3 mm continuum emission from Y. Cheng et al. (2022). Due to their non-detection at 6 cm, we

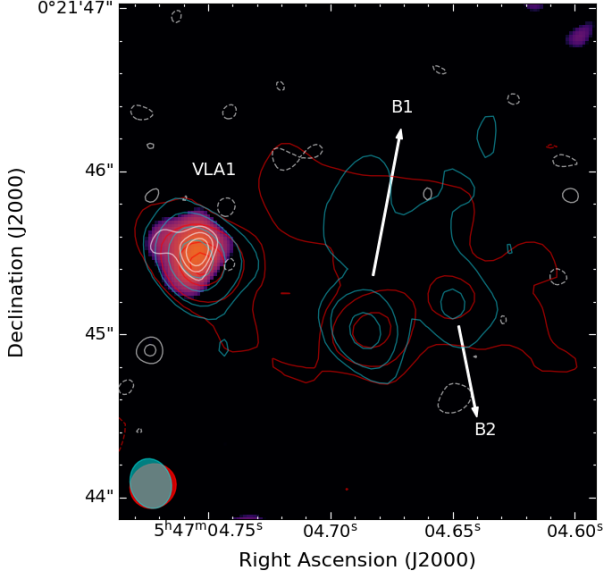


Figure 4. VLA 3.6 continuum map and contours (white) from Fig. 1 in C. Carrasco-González et al. (2012) (see more details on their paper regarding the radio maps), of the radio source VLA 1 in the NGC 2071 region with VLA contours overlaid (1.3–cyan, 3.6–white, and 6 cm–red). The contour levels are at $[-3, 3, 5, 10, 50, 100] \times 13.7 \mu\text{Jy/beam}$ for 1.3 cm (K-band), at $[-3, 3, 5, 7, 10, 15, 20, 40, 60] \times 30 \mu\text{Jy/beam}$ for 3.6 cm, and at $[-3, 3, 5, 15, 60, 120] \times 7.6 \mu\text{Jy/beam}$ for 6 cm (C-band). The beam sizes are indicated in the lower left-hand corner.

estimate upper limits on their spectral indices: $\alpha \lesssim 1.1$ for HOPS-361-E-cm and $\alpha \lesssim 0.7$ for IRS 8-cm. Given their spectral properties and millimeter associations, we suggest these are likely individual YSOs within the NGC 2071 cluster.

3.1.4. Cepheus E

Cepheus E is a molecular cloud at a distance of 730 pc (A. I. Sargent 1977) whose central source, the isolated intermediate-mass Class 0 protostar Cep E-mm (B. Lefloch et al. 1996; A. Moro-Martín et al. 2001), drives a molecular outflow and jet, as revealed by CO(2-1) and CO(3-2) maps (B. Lefloch et al. 2011, 2015). The southern jet terminates at the bright Herbig–Haro object HH 377 (S. Ayala et al. 2000; A. Gusdorf et al. 2017). J. Ospina-Zamudio et al. (2018) detected a hot corino in Cep E-mm and resolved it into a binary system (Cep E-A and Cep E-B), using NOEMA observations at 1.3 and 3.3 mm with resolutions of $\sim 1.4''$ and $\sim 2.4''$, respectively. With their mm data, J. Ospina-Zamudio et al. (2018) concluded that both millimeter components drive high-velocity molecular jets, with Cep E-A powering the jet associated with HH 377, and Cep E-B powering another jet almost perpendicular to the Cep E-A

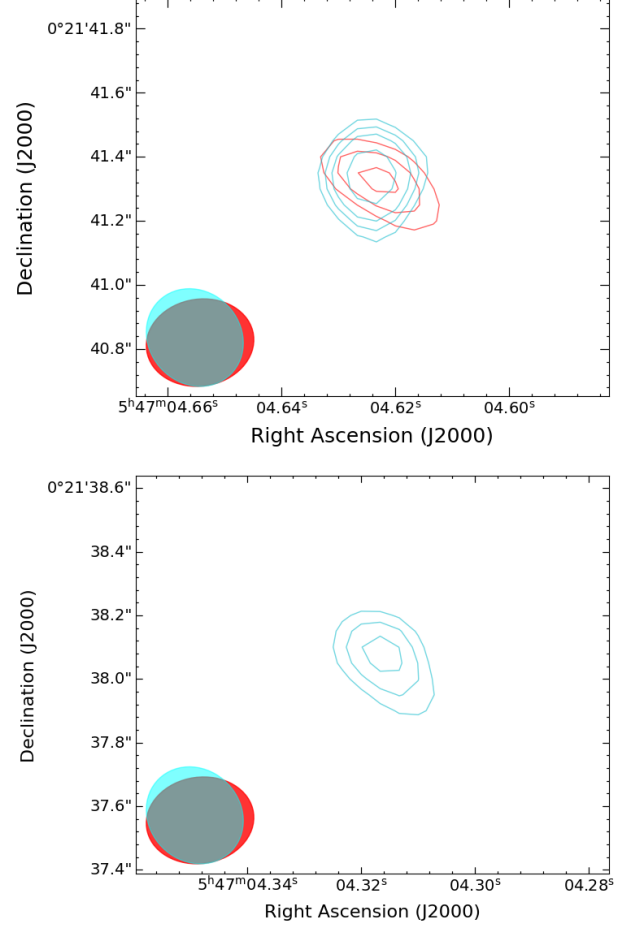


Figure 5. VLA continuum maps of the radio sources: HOPS-361-E-cm (top) and IRS 8 (bottom) in the NGC 2071 region observed at 1.3 cm (cyan) and 6 cm (red). The contour levels are at $[-3, 3, 4, 5] \times 7.6 \mu\text{Jy/beam}$ for 1.3 cm (K-band), and at $[-3, 3, 4, 5, 7] \times 13.7 \mu\text{Jy/beam}$ for 6 cm (C-band). The beam sizes are indicated in the lower left-hand corner.

jet. J. Ospina-Zamudio et al. (2019) identified several molecular species in the Cep E-A jet, including SO, SiO, H_2CO , CS, HCO^+ , and HCN.

From our observations, we detect a compact source at K band (1.3 cm) and only a 3σ detection at C band, representing, to our knowledge, the first reported centimeter detection toward this source. The emission is coincident with Cep E-mm, previously detected in the infrared and millimeter (B. Lefloch et al. 1996, 2015; A. Moro-Martín et al. 2001), but at our resolution the binary components are not resolved and it appears we are only resolving Cep E-A. We estimate a lower limit to the spectral index of $\alpha > 2.1$.

This source exhibits several star-formation tracers, such as a mm counterpart, molecular outflows, and a rich variety of molecular species associated with the jet

powered by Cep E-A. Since this source is detected only at K band and we report a lower limit for its spectral index, the current evidence is insufficient to draw a firm conclusion about its nature. Further observations are needed to determine it with more certainty.

3.1.5. *L1206*

L1206, also known as IRAS 22272+6358, is a region located at a distance of 776 pc (K. L. J. Rygl et al. 2010). In SOMA III, two MIR sources are presented in the field of view separated at distance of about 40". Consequently, our analysis focuses on the L1206 A and L1206 B regions, where we present 6 and 1.3 cm observations.

L1206 A: Region L1206 A presents a CO molecular outflow at the position of the source OVRO 2 (IRAS 22272+6358A hereafter referred to as L1206 A) (M. T. Beltrán et al. 2006; D.-J. Liu et al. 2021). Moreover, G. Surcis et al. (2013) with VLBI observations, detected 26 6.7-GHz methanol (CH₃OH) masers features towards L1206 A and aligned in the direction of the molecular outflow.

The source L1206 A, has no optical counterpart, but has been observed at infrared, millimeter (2 and 2.7 mm) and radio continuum wavelengths in the Q (0.7 cm) and C bands (K. Sugitani et al. 2000; M. T. Beltrán et al. 2006; S. J. D. Purser et al. 2021). M. T. Beltrán et al. (2006) suggested that the intermediate-mass protostar, L1206 A is in a transition between a Class 0 and I object, giving the dust emission morphology and properties of OVRO 2. Meanwhile, S. J. D. Purser et al. (2021) suggested that L1206 A traces an ionized jet (candidate) at 6 cm (C-band), but is dominated by disk emission at Q-band.

In our 6 and 1.3 cm observations, we report a single detection that is coincident with the source A and OVRO 2 reported by S. J. D. Purser et al. (2021) and M. T. Beltrán et al. (2006) respectively. This source presents an interesting morphology. At 6 cm (C-band), it shows an elongation in the N-S direction, but at higher sigma levels and at 1.3 cm (K-band), it displays a compact morphology. We report an estimate spectral index of $\alpha \sim 0.9$, which is similar to the value reported by S. J. D. Purser et al. (2021) of $\alpha \sim 1.05$. Given the morphology of the source, the weak centimeter emission and a spectral index of $\alpha \sim 1$, we are in accordance with S. J. D. Purser et al. (2021) and conclude that L1206 A appears to be ionized jet. We also report that source L1206 A presents a 6.7 GHz methanol (CH₃OH) maser within the synthesized beam, with a flux density around 2.88 mJy.

L1206 B: Source IRAS 22272+6358 B (hereafter referred to as L1206 B) is a less luminous object that lies 40" to the east of L1206 A and is clearly visible at near infrared wavelengths. M. E. Ressler & M. Shure (1991) suggested that L1206 B is a late Class I object or an early Class II object.

For source L1206 B, we present the first radio observations (to the knowledge of the authors) of this region and we report a single compact detection with an estimated spectral index of $\alpha \sim 1.1$ that may indicate free-free emission from an ionized jet or an optically thick HC HII region (V. Rosero et al. 2019b), although higher resolution observations are needed to confirm either scenario.

3.1.6. *IRAS 22172+5549*

IRAS 22172+5549 is located at 2.4 kpc (S. Molinari et al. 2002) and hosts a range of YSOs, from intermediate- to high-mass protostars deeply embedded in massive dense cores (A. Palau et al. 2013). Our analysis focuses on the MIR1, MIR2, and MIR3 regions identified by S. Molinari et al. (2002). F. Fontani et al. (2004) reported a CO(1-0) bipolar outflow centered on MIR2 (also known as IRS1), whose parameters suggest a relatively massive protostar. M. Liu et al. (2020) also detected extended emission along the blue-shifted lobe of this outflow using SOFIA observations. For MIR1 and MIR3, no mm emission or molecular outflows have been reported (F. Fontani et al. 2004; A. Palau et al. 2013).

In our VLA observations, none of the MIR sources from S. Molinari et al. (2002) are detected, consistent with S. J. D. Purser et al. (2021), whose similar-resolution and sensitivity data revealed only one C-band (6 cm) source, but which was not coincident with any MIR positions, and no Q-band (0.7 cm) detections.

3.1.7. *IRAS 21391+5802*

IRAS 21391+5802 is a young, intermediate-mass object deeply embedded in the bright-rimmed globule IC 1396N at a distance of 750 pc (H. I. Matthews 1979). This source shows strong submillimeter and millimeter continuum dust emission (B. Wilking et al. 1993), high-density gas (C. Codella et al. 2001), and water maser emission (R. Valdetaro et al. 2005).

M. T. Beltrán et al. (2002) resolved the source into three millimeter cores—BIMA 1, BIMA 2, and BIMA 3—associated with centimeter sources VLA 1, VLA 2, and VLA 3, respectively, detected using 3.6 cm observations. BIMA 2 is an IM protostar surrounded by the less massive BIMA 1 and BIMA 3, and it drives a strong east–west molecular outflow. R. Choudhury et al.

(2010) identified ~ 45 YSOs in IC 1396N from NIR observations, with MIR 50 and MIR 54 corresponding to BIMA 2 and BIMA 3, and MIR 48 located $\sim 45''$ north of BIMA 2.

Our analysis focuses on BIMA 2, BIMA 3, and MIR 48. We detect multiple radio sources toward BIMA 2 and BIMA 3, but no emission toward MIR 48. The latter result is consistent with the results shown

by M. T. Beltrán et al. (2002), who did not detect any source around MIR 48 at 3.6 cm with a resolution of $17''.9$ and a sensitivity of $32 \mu\text{Jy}$. Table 7 summarizes the multiplicity in BIMA 2 and BIMA 3, including the R.A. and Decl. positions, estimated spectral indices, associations at other wavelengths, whether each source represents a new radio detection, and the estimated spectral type (more details about this are presented in Sect. 4.1).

Table 7. Multiplicity in IRAS 21391 BIMA 2 and BIMA 3.

Region	Source	R.A. (J2000)	Decl. (J2000)	Spectral Index	Association	New Detection	Spectral Type
BIMA 2	VLA 2A	21:40:41.86	+58.16.11.95	0.7 (0.09)	mm	Yes ^a	B3
	VLA 2B	21:40:41.73	+58.16.12.81	0.9 (0.66)	mm	Yes ^a	B3
	VLA 2C	21:40:41.73	+58.16.14.34	1.2 (0.18)	mm	Yes ^a	B4
BIMA 3	VLA 3	21:40:42.84	+58.16.01.36	0.9 (0.16)	IR, mm	No	B3
	VLA 3B	21:40:43.46	+58.15.59.49	0.0 (0.20)	...	Yes ^b	B4

NOTE— Units of R.A. are hours, minutes, and seconds. Units of decl. are degrees, arcminutes, and arcseconds.

^a These sources have been previously detected in radio continuum but we are resolving into multiple detections

^b These sources have been observed but not detected.

IRAS 21391+5802 BIMA2: To our knowledge, this is the first time source VLA 2 has been resolved into three components. We detect emission at both C and K bands, labeling the components VLA 2A, VLA 2B, and VLA 2C. These ionized sources are associated with the millimeter cores IRAM 2A, 47.73+14.3, and 47.73+12.8 reported by R. Neri et al. (2007) using 3.3 and 1.3 mm observations with resolutions of $\sim 0.45''$ and $\sim 1.0''$, respectively. Their association supports the interpretation that each source is ionized by an independent protostellar object.

The central source, VLA 2A, is relatively compact, as its north–south elongation aligns with the beam direction. Sources VLA 2B and VLA 2C appear as point sources. The reported positive spectral indices, consistent with thermal emission, together with their spectral types (see Table 7) and association with millimeter emission, provide further evidence that these three sources are independent protostellar objects.

IRAS 21391+5802 BIMA3: We detect two sources at both 1.3 cm and 6 cm. The first, VLA 3, was previously reported by M. T. Beltrán et al. (2002), who classified it as an evolved low-mass object based on its compact morphology and small dust emissivity index. In our data, VLA 3 appears slightly elongated in the NE–SW direction.

We also identify a second compact source, located east of VLA 3 at around $10''$ and labeled VLA 3B, which, to

our knowledge, has not been previously reported. This source has no known counterparts at other wavelengths.

We report an estimated spectral index of $\alpha \sim 0.9$ for VLA 3, which denotes the presence of thermal emission and is in the range of expected spectral index for ($0.2 \leq \alpha \leq 1.2$) ionized jets (V. Rosero et al. 2019b; G. Anglada 1995). For source VLA 3B we report a flat spectral index of $\alpha \sim 0.0$.

Given the slightly extended morphology, the mm counterpart, and the estimated spectral index of VLA 3, we suggest that the nature of this source is an ionized jet; however, more information and additional observations are needed to confirm this assessment. Another possibility is that this source could be a protostellar object with a B3 spectral type, as shown in Table 7

Meanwhile, source VLA 3B is too far from VLA 3 to be considered associated with it. Furthermore, there is no mm counterpart in the high-resolution 1.3 and 3.3 mm observations reported by R. Neri et al. (2007). Considering all this and given the compact morphology of this source, its nature could be extragalactic, but more information and observations are still required to confirm this assessment.

3.2. Radio SEDs

In Figure 6 we present the extended (E-)SEDs, i.e., radio + IR SEDs, for our twelve sources. The dashed lines correspond to the best fit to the data using a power law of the form $S_\nu \propto \nu^\alpha$, where α is the spectral index at

the different scales: *SOMA*, *Intermediate*, and *Inner*, as described above. The spectral index was calculated using the flux density at the central frequencies of the images, so α is calculated over a wide frequency range (~ 20 GHz). The uncertainty in the spectral index was calculated with a Monte Carlo simulation that bootstrapped the flux density uncertainties. We estimated an upper limit in the spectral index for non-detections at higher frequencies using a value of S_ν of 3σ .

It is important to mention that at higher frequencies (1.3 cm) the fluxes are most likely measuring the combination of dust and free-free emission (see [C. L. Brogan et al. \(2016\)](#) for more details), therefore adding some systematic errors to the measurement of the fluxes.

4. ANALYSIS AND DISCUSSION

To better understand the nature of the sources from radio observations, we analyze the morphology, multiplicity, and spectral indices of the *SOMA* III sample. Unlike the sources in *SOMA Radio I* and *SOMA Radio II*, our targets are mostly located within 1 kpc, except for S235 and IRAS 22172+5549, and generally exhibit low radio flux densities. Among the twelve sources studied, only NGC 2071 shows flux densities above 3 mJy.

Following the approach of Section 4.2 in *SOMA Radio II*, we use VLA observations to assess the nature of each source based on morphology, spectral index and their association with any tracers of star formation. For objects with previous studies, we draw on earlier characterizations, comparing them with our measurements (see §3.1 for individual analyses). This comparison refines our understanding of the underlying radio emission mechanisms in each case.

4.1. Multiplicity and source characterization

Across the 12 regions analyzed, we detected 18 sources in total. Multiplicity is present in only three cases: NGC 2071 (eight sources), IRAS 21391+5802 BIMA2 (three sources), and IRAS 21391+5802 BIMA3 (two sources). Compared to *SOMA Radio I*; *SOMA Radio II*, the sample of intermediate-mass protostars analyzed in this work shows a significantly lower multiplicity, with only 3 of 12 regions (25%) showing multiple sources, while the earlier studies reported multiple detections in 14 of 17 regions ($\sim 82\%$).

Of the 18 detections, four are entirely new, with no counterparts at any wavelength, and four are new radio detections of sources previously identified at other wavelengths. We also resolve IRAS 21391+5802 BIMA2 into three distinct components, each with a millimeter counterpart, which we consider new radio detections.

We identify four regions—IRAS 22172+5549 MIR1, MIR2, and MIR3, and IRAS 21391+5802 MIR48, where

Table 8. Parameters from Radio Continuum at the sensitivity limit at 5 GHz.

Region	$\log N'_{\text{Ly}}^{\text{a}}$	Sp ^b	M_{\odot}^{c}
S235	42.93	B3	5.4
IRAS 22198+6336	42.14	B4	5.1
NGC 2071	41.99	B4	5.1
Cepheus E	42.04	B4	5.1
L1206 A	42.25	B4	5.1
L1206 B	42.23	B4	5.1
IRAS 22172+5549 MIR1	43.34	B3	5.4
IRAS 22172+5549 MIR2	43.33	B3	5.4
IRAS 22172+5549 MIR3	43.37	B3	5.4
IRAS 21391+5802 BIMA2	42.14	B4	5.1
IRAS 21391+5802 BIMA3	42.20	B4	5.1
IRAS 21391+5802 MIR48	42.22	B4	5.1

NOTE—

^a Values calculated using equations from [S. Kurtz et al. \(1994\)](#); [N. Panagia & C. M. Walmsley \(1978\)](#).

^b Spectral type estimation made from extrapolating the values in table II in [N. Panagia \(1973\)](#).

^c The estimate of the mass was taken from [M. J. Pecaut & E. E. Mamajek \(2013\)](#)

no sources are detected at the 5σ level. Following the methodology of *SOMA Radio II*, and in order to determine if we are missing any UCHII regions, we estimate the physical properties implied by the 5 GHz sensitivity limit (rms) using equations (1) and (3) from [S. Kurtz et al. \(1994\)](#) and equation (A.2.3) from [N. Panagia & C. M. Walmsley \(1978\)](#).

These calculations assume spherical symmetry and optically thin emission from a uniform-density plasma with $T_e = 10^4$ K. The results are presented in Table 8, where column 1 lists the region name, column 2 gives the logarithm of the Lyman continuum flux ($\log N'_{\text{Ly}}$) required for ionization, and column 3 shows the corresponding spectral type from Table II of [N. Panagia \(1973\)](#), assuming a single ZAMS star is responsible for the ionization. For cases where we obtain B4 spectral types, we use an extrapolation from the values in Table II of [N. Panagia \(1973\)](#), since the minimum value of the logarithm of the Lyman continuum flux ($\log N'_{\text{Ly}}$) in that table is 43.69 (for a B3 spectral type). The distances used in these calculations are taken from Table 1. Column 4 lists the stellar mass associated with each spectral type, from [M. J. Pecaut & E. E. Mamajek \(2013\)](#).

From Table 8 we can derive an estimation of the lowest mass ZAMS star that we can detect with the sensitivity of our observations. Therefore, we use this estimate as a completeness parameter on the multiplicity at the

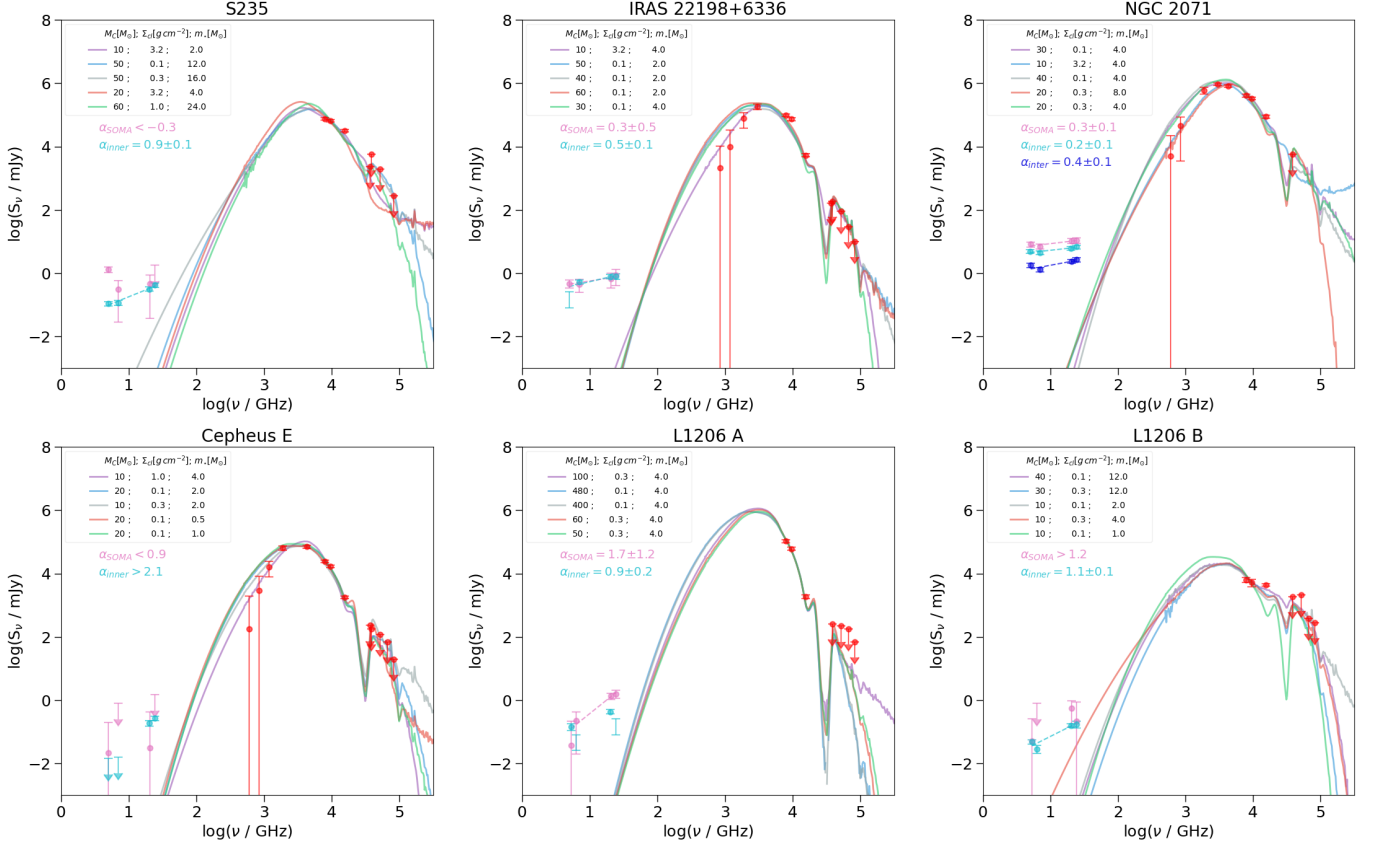


Figure 6. Extended spectral energy distributions (E-SEDs) of SOMA protostars, consisting of radio and IR SEDs. The circles correspond to the flux density as a function of the frequency at each scale (magenta: *SOMA*; blue: *Intermediate*; cyan: *Inner*). Error bars are explained in §3.2. The solid lines show the five best fits (see legend) to the IR data SED from the Y. Zhang & J. C. Tan (2018) models as fit by *SOMA V* (see table C1, Appendix in *SOMA V*), and the dashed lines are the best fit of the radio data using a power law of the form $S_\nu \propto \nu^\alpha$.

different regions, especially for the regions where we do not report any detection.

4.2. Nature of the radio emission

By leveraging previous studies on the sources in this sample, as well as the results from our radio observations, we have assessed the nature of each individual source (see §3.1 for more details). From the 18 sources we report in this paper, it is important to highlight that 6 are radio jets given their morphology and the estimated spectral index. IRAS 22198+6336 and the sources IRS1 and IRS3 in NGC 2071, are examples of previously studied ionized jets. All three exhibit a jet-like morphology and a spectral index in the range for typical ionized jets associated with YSOs (S. P. Reynolds 1986; G. Anglada et al. 1998; K. E. I. Tanaka et al. 2016). Additionally, we suggest that sources L1206 A, L1206 B and IRAS 21391+5802 BIMA3 VLA-3 could be ionized jets given their morphology, weak centimeter emission and spectral index values consisted with ion-

ized jets associated with YSOs. However, further studies are needed for a definitive interpretation of their nature.

Similarly, we have NGC 2071 VLA1, which was previously classified as a younger and more embedded YSO than the other sources associated in the region. From our results, and based on previous studies, we agree with the scenario that this source has a radio jet given the jet-like morphology, the spectral index and two thermal components (VLA 1-B1 and VLA 1-B2) that are aligned in the direction of the jet. More observations are needed to fully resolve the sources and confirm the nature of this proposed radio jet.

Regarding the remaining sources in NGC 2071, IRS 1Eb exhibits a relatively flat spectral index, indicating thermal emission. Its proximity to the radio jet IRS 1 suggests that this source might be part of the jet emission. The two new radio detections, HOPS-361-E-cm and IRS 8 cm, have mm counterparts, and their compact morphology and positive spectral indices suggest that they are likely individual YSOs within the NGC 2071 cluster. Similarly, the three sources toward

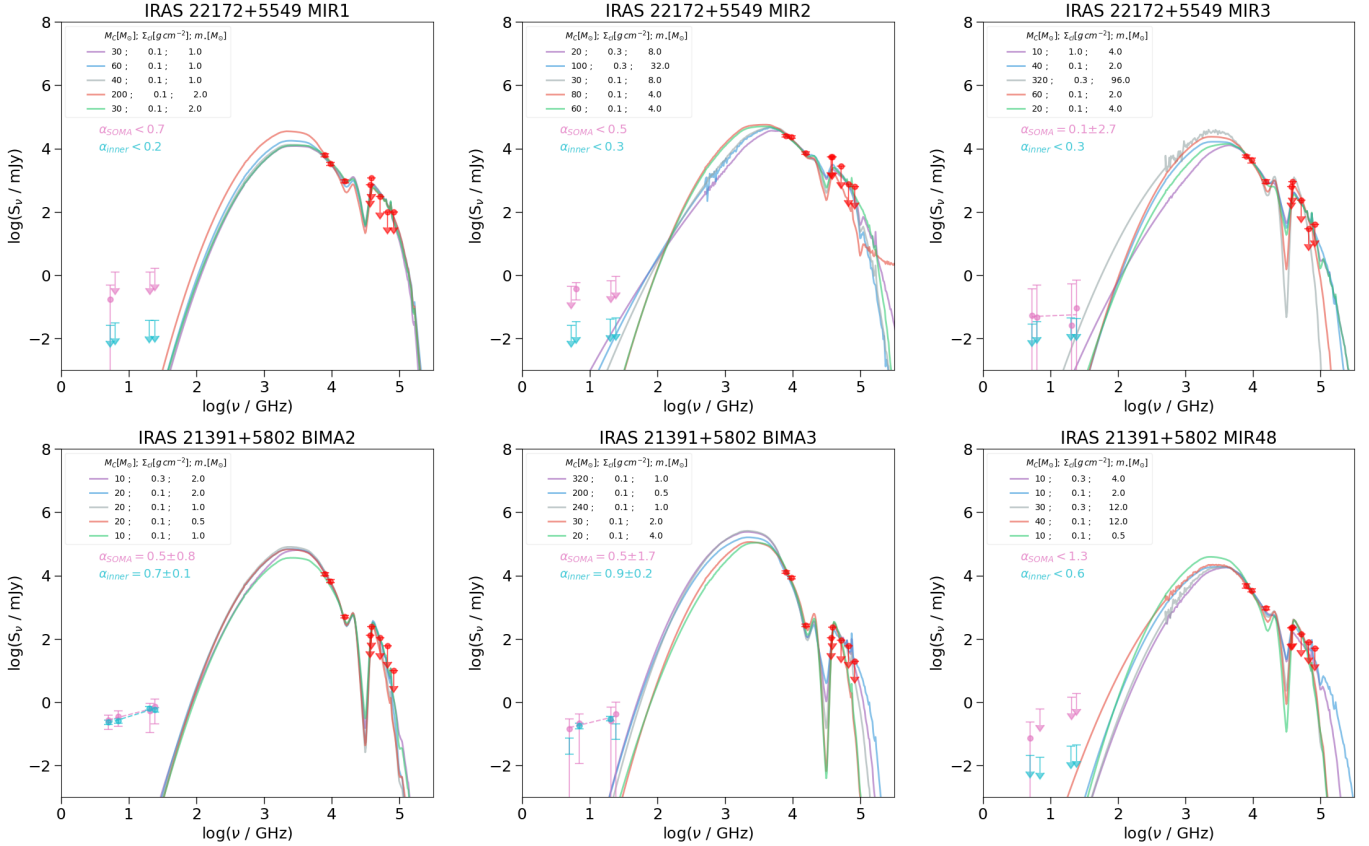


Figure 6. (Continued)

IRAS 21391+5802 BIMA2 (VLA 1, 2, and 3) show evidence of being individual YSOs. In this case, the most likely scenario is that source VLA 2 is the most massive and is driving the molecular outflow. Source S235 was classified as a Herbig Be star by [P. A. Boley et al. \(2009\)](#). Our results, which show a compact morphology and a spectral index consistent with thermal emission, support this conclusion regarding the nature of the source. Table 9 summarizes the detections and the corresponding assessments of the nature of each source.

In [SOMA Radio I](#) and [SOMA Radio II](#), we reported different evolutionary stages and nature of the sample, which included radio jets, UC HII regions, and variable stars. In general, 9 of the 17 regions previously analyzed presented characteristics that indicated a radio jet scenario. In this work, we present a slightly lower distribution with only 4 (IRAS 22198+6336, NGC 2071, L1206 A and L1206 B) of the 12 regions exhibiting characteristics consistent with radio jets, since 3 (NGC 2071: IRS1, IRS3, and VLA1) of the 6 radio jet scenarios that we report are from sources associated with region NGC 2071. Given our sensitivity limit, we also identify 4 regions where we do not report a 5σ detection (IRAS 22172+5549: MIR1, MIR2, and MIR3, and

IRAS 21391+5802 MIR48), in contrast to the first 17 regions analyzed, where only one, IRAS 16562-3959 N from [SOMA Radio II](#), was a non-detections.

4.3. Radio - bolometric luminosity of IM protostars

Following the results from [SOMA Radio II](#), in Figure 7 we present the radio luminosity at 5 GHz from the *Inner* (left panel) and *SOMA* (right panel) scales versus the bolometric luminosity. For the bolometric luminosity of SOMA sources (detections from SOMA I and II samples are magenta and blue squares, respectively) we report the average of the “good” models from Table C1 of [SOMA V](#) and the error bar for the [SOMA III](#) sources corresponds to the dispersion of these good models. We also show data for lower-mass YSOs associated with ionized jets from [G. Anglada \(1995\)](#) (small yellow dots). We scaled their fluxes from 3.6 cm, using a factor of 0.74, assuming that these sources have a spectral index $\alpha = 0.6$, which is the expected value of ionized jets. A power-law fit to these data of $(S_\nu d^2 / [\text{mJy kpc}^2]) = 8 \times 10^{-3} (L_{\text{bol}} / L_\odot)^{0.6}$ is shown with a dashed line. UC/HC HII regions from [S. Kurtz et al. \(1994\)](#) are represented with a \times symbols. Note, the bolometric luminosities of the low-mass YSOs

Table 9. Summary of the nature of the sources reported in the [SOMA III](#) sample.

Region	Source	Nature
S235	VLA-2	Herbig Be star
IRAS 22198+6336	VLA2	Ionized Jet
NGC 2071	IRS 1	Jet Candidate
NGC 2071	VLA 1	Jet Candidate
NGC 2071	VLA 1-B1	Jet Knot (Candidate)
NGC 2071	VLA 1-B2	Jet Knot (Candidate)
NGC 2071	IRS 1Eb	Jet Knot (Candidate)
NGC 2071	IRS 8-cm	YSOs
NGC 2071	HOPS-361-E-cm	YSOs
NGC 2071	IRS 3	Jet Candidate
Cepheus E	VLA1	Undetermined
L1206 A	A	Jet Candidate
L1206 B	B	Jet Candidate or HC HII Region
IRAS 21391+5802 BIMA2	VLA 2A	YSOs
IRAS 21391+5802 BIMA2	VLA 2B	YSOs
IRAS 21391+5802 BIMA2	VLA 2C	YSOs
IRAS 21391+5802 BIMA3	VLA 3	Jet Candidate or YSOs
IRAS 21391+5802 BIMA3	VLA 3B	Undetermined

and the UC/HC HII regions are not measured in exactly the same way as the SED-fitting method of the SOMA sources, for which we are reporting intrinsic bolometric luminosities of the fitted SED models. Similar to [SOMA Radio II](#), a plot showing the results based on isotropic bolometric luminosities is presented in Appendix A.

Several theoretical models for the radio luminosity of massive protostars are plotted in Figure 7. The black dotted line is the radio emission expected from an optically thin HII region, given the Lyman continuum luminosity of a single zero age main sequence (ZAMS) star at a given bolometric luminosity ([R. I. Thompson 1984](#)). The light blue lines correspond to the models from [TTZ16](#), of the expected radio emission that arises from photoionization of a massive protostar forming via Turbulent Core Accretion (TCA), also for optically thin conditions at 5 GHz. These models have an initial core mass of $M_c = 60 M_\odot$ and the three cases correspond to clump environment mass surface densities of $\Sigma_{cl} = 0.316, 1$ and 3.16 g cm^{-2} . The lower mass surface densities correspond to lower accretion rates, for which protostellar contraction towards the ZAMS occurs sooner, i.e., at lower masses and lower values of L_{bol} . Note, these models do not include any contribution from shock ionization. Similar plots with an additional sets of theoretical models based on optically thin radio emission from the ionizing photon output of the TCA protostellar evolution models of [Y. Zhang & J. C. Tan \(2018\)](#) are shown in Appendix B.

[E. C. Gardiner et al. \(2024\)](#) developed a model for estimating the radio emission from free-free emission from ionized gas produced by collisional ionization in shocks for a massive protostar forming from a $60 M_\odot$ core in a 1 g cm^{-2} clump environment. This radio emission is also shown in Figure 7 with dark blue lines. We note that the contribution from shock ionization is quite spatially extended, with the emission from a 25,000 au radius aperture (more closely matching the SOMA scale) being about a factor of 10 higher than that from a 1,000 au aperture (more closely matching the inner scale).

As in [SOMA Radio II](#), it is important to note that, at the SOMA scale, we may miss radio flux due to interferometric filtering. The SOMA scale (right plot) captures all the emission in the region, including contaminating contributions from jet knots and other nearby sources, further enhancing the radio luminosity. The artificial flux added by these sources, along with the differing spatial scales relative to the inner scale, makes the SOMA scale less reliable for assessing the intrinsic nature of individual sources. However, but the SOMA scale still holds importance since it allows direct comparison with theoretical models with bigger scales that take into account jet knots and other multiple stellar sources in proto-clusters.

The differences between the results shown in the two plots of Figure 7 (as well as Figures A1, B1, and B2), particularly for the sources we classified as having jet-like morphologies (IRAS 22198+6336, NGC 2071, L1206

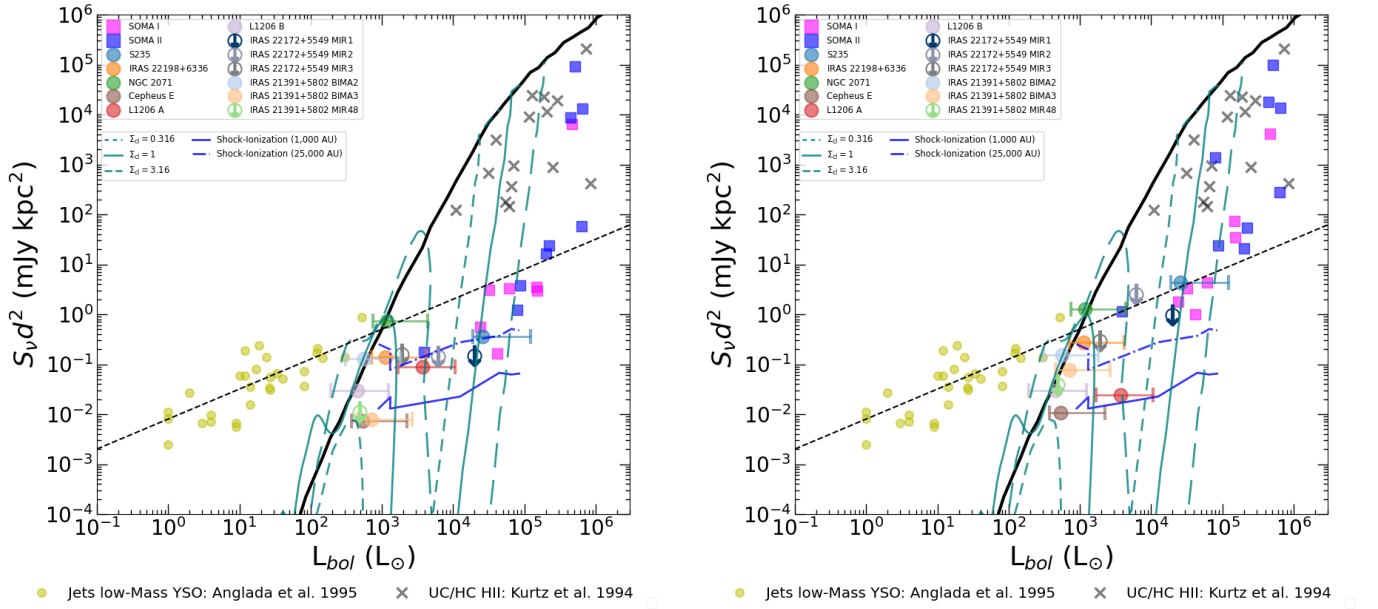


Figure 7. Radio luminosity at 5 GHz for the Inner scale (left) and for the SOMA scale (right) as a function of the bolometric luminosity of for 29 SOMA sources from SOMA Radio I and II (squares) and III (circles) (see legend). In each panel we also show lower-mass YSOs from [G. Anglada \(1995\)](#) (small yellow circles). The dashed line shows a power-law fit to these lower-mass YSOs ([G. Anglada et al. 2015](#)): $(S_\nu d^2 / [\text{mJy kpc}^2]) = 8 \times 10^{-3} (L_{\text{bol}} / L_\odot)^{0.6}$. The \times symbols are HC and UC HII regions from [S. Kurtz et al. \(1994\)](#). The black solid line shows the radio emission expected from optically thin HII regions powered by ZAMS stars ([R. I. Thompson 1984](#)). The light blue lines show models for HII regions powered by TCA model protostars ([K. E. I. Tanaka et al. 2016](#)) (with $M_c = 60 M_\odot$ and $\Sigma_{\text{cl}} = 0.316, 1$ and 3.16 g cm^{-2} , as labeled). Note that these models, which do account for radiative transfer effects of the free-free emission, assume that all of the ionizing photons are reprocessed by the HII region, i.e., with zero escape fraction. The dark blue lines show radio emission from shock ionization in simulations of a fiducial TCA protostar, i.e., forming from a $60 M_\odot$ core in a 1 g cm^{-2} clump environment ([E. C. Gardiner et al. 2024](#)), with the solid and dot-dashed lines showing emission from within 1,000 and 25,000 au of the protostar, respectively.

A and L1206 B), arise from the different scales used to determine the radio luminosity ([Ü. Kavak et al. 2021](#)).

With the addition of the **SOMA III** sample, which is composed of intermediate-mass protostars, we now present a total of 29 SOMA protostars that expand the range of the radio versus bolometric luminosity relation. Our data points now cover values from $L_{\text{bol}} \sim 10^2$ to $10^6 L_\odot$. This large range of observations is important for studying the relationship between protostellar models and the observations.

Comparing the distribution of the **SOMA III** radio sources with the models, we find that our sample is considerably less luminous than the **SOMA I** and **SOMA II** sources. As expected, the sources analyzed in this work (intermediate-mass protostars) are positioned between the lower-mass YSOs from [G. Anglada \(1995\)](#) and the more massive sources from our current sample, except for S235, which is closer to the massive sources but is still at the lower end of the high-mass stars in our sample. For a more in-depth analysis of the **SOMA I** and **SOMA II** sources, please refer to Sections 6 and 4 of

SOMA Radio I and **SOMA Radio II**, respectively. It is important to note that most of our intermediate-mass protostars present lower radio luminosities than the low-mass protostars reported by [G. Anglada et al. \(2015\)](#), and therefore most of our points fall below the dashed line at both the inner and the SOMA scale.

By expanding the SOMA protostar sample, we see that the behavior described in **SOMA Radio II** still holds, namely that the sources exhibit relatively faint radio luminosities compared to the predictions of protostellar models. The addition of the intermediate-mass protostars strengthens the suggestion that the rise in ionizing luminosity may occur only at relatively higher protostellar masses and luminosities. Moreover, we find that the radio luminosity measured on the SOMA scale rises steeply, by about three dex, as the bolometric luminosity increases by one dex. This rise is smaller than that found in the more massive protostars (**SOMA II**), but is still considered a steep increase, consistent with the basic expectations of TCA massive protostar models. Additionally, we see that the shock ionization model

of [E. C. Gardiner et al. \(2024\)](#), which falls below the extrapolated lower-mass YSO relation, is generally consistent with most of the sources in the SOMA III sample.

The addition of the IM protostars to the SOMA Radio sample reveals a deviation from the power law extrapolation of radio luminosity from low-mass protostars. The radio faintness of IM protostars is consistent with predictions of protostellar evolution models with $\Sigma_{\text{cl}} \lesssim 1 \text{ g cm}^{-2}$: in the range of luminosities from $\sim 3 \times 10^2 L_{\odot}$ to $\sim 10^4 L_{\odot}$ the protostars produce very little photoionization since they are in an expanded, relatively cool state. Thus shock ionization is still expected to dominate in this regime, but the models of [E. C. Gardiner et al. \(2024\)](#) indicate this emission may be relatively weak, likely because outflow speeds are also reduced given the expanded protostellar radii.

5. SUMMARY AND CONCLUSIONS

Following the work done in [SOMA Radio I](#) and [SOMA Radio II](#), we present results from radio continuum VLA follow-up observations of the [SOMA III](#) sample, which is primarily composed of intermediate-mass protostars. These observations allow us to precisely locate the protostars, investigate multiplicity, and identify ionized gas emission. The latter provides insight into outflow morphology, particularly through the orientation of radio jet axes, and serves as a potential evolutionary indicator for massive protostars, especially as they approach the zero-age main sequence, when photoionization is expected to play an increasingly dominant role. With the addition of the 12 sources in the 7 target region, our SOMA Radio sample now is composed of 29 sources, covering values from $L_{\text{bol}} \sim 10^2$ to $10^6 L_{\odot}$. Below, we summarize our main findings:

- We detected 18 sources in the 12 regions that are part of the [SOMA III](#) sample, but we find multiplicity (e.g. two or more detections 5σ within the SOMA scale) in only 3 of these 12 regions (NGC 2071, IRAS 21391+5802 BIMA2, and IRAS 21391+5802 BIMA3). Moreover, we present 4 regions where we do not report a detection above our 5σ threshold (IRAS 22172+5549: MIR1, MIR2, and MIR3, and IRAS 21391+5802 MIR48).
- Similar to [SOMA Radio I](#) and [SOMA Radio II](#), we report a variety of nature and evolutionary stages for the sources in the sample, with 7 out of the 18 sources being classified as ionized jet candidates given their morphologies and spectral indices.
- We find the [SOMA III](#) sample to be considerably less luminous than the [SOMA I](#) and [SOMA II](#) sources, and, as expected, these IM protostars are positioned between the lower-mass YSOs from [G. Anglada \(1995\)](#) and the more massive sources from the [SOMA I](#) and [SOMA II](#) sample.
- The IM protostars present lower radio luminosities than would be expected from a power law extrapolation from the low-mass protostars reported by [G. Anglada et al. \(2015\)](#), which is consistent with the theoretically expected low photoionization rate. The shock ionization model of [E. C. Gardiner et al. \(2024\)](#), which also falls below the extrapolated lower-mass YSO relation, is generally consistent with most of the sources in the [SOMA III](#) sample.
- The broad range of observations enables us to directly connect protostellar models with observations, providing new constraints on theories of massive protostar ionization and offering deeper insight into how ionization is tied to protostellar structure and evolutionary stage.

ACKNOWLEDGMENTS

The authors would like to thank Prof. Carlos Carrasco-González for providing the additional VLA images of source NGC 2071 originally presented in [C. Carrasco-González et al. \(2012\)](#). F. S. M. acknowledges support from the NRAO NINE (National and International Non-traditional Exchange) program. V. R. acknowledges support from NSF grant AST-2206437 to the Space Science Inst. J.C.T. acknowledges support from NSF grant AST-2206437 and ERC Advanced Grant 788829 (MSTAR). R.F. acknowledges support from the grants PID2023-146295NB-I00, and from the Severo Ochoa grant CEX2021-001131-S funded by MCIN/AEI/ 10.13039/501100011033 and by “European Union NextGenerationEU/PRTR”. The National Radio Astronomy Observatory and Green Bank Observatory are facilities of the U.S. National Science Foundation operated under cooperative agreement by Associated Universities, Inc.

Facility: VLA

Software: CASA ([J. P. McMullin et al. 2007](#)), Astropy ([Astropy Collaboration et al. 2013, 2018](#)), APLpy ([T. Robitaille & E. Bressert 2012](#); [T. Robitaille 2019](#))

6. ORCID IDS

F. Sequeira-Murillo

<https://orcid.org/0000-0001-8169-1437>

V. Rosero <https://orcid.org/0000-0001-8596-1756>
 J. Marvil <https://orcid.org/0000-0003-1111-8066>
 J. C. Tan <https://orcid.org/0000-0002-3389-9142>
 R. Fedriani <https://orcid.org/0000-0003-4040-4934>
 Y. Zhang <https://orcid.org/0000-0001-7511-0034>

P. Gorai <https://orcid.org/0000-0003-1602-6849>
 J. M. De Buizer <https://orcid.org/0000-0001-7378-4430>
 M. T. Beltran <https://orcid.org/0000-0003-3315-5626>

APPENDIX

A. RADIO LUMINOSITY VERSUS ISOTROPIC BOLOMETRIC LUMINOSITY

Figure A1 shows a similar plot to Figure 7, but in this case we used the average of the good models of the isotropic bolometric luminosity (Table C.1 of SOMA V). Everything else is the same as Figure 7.

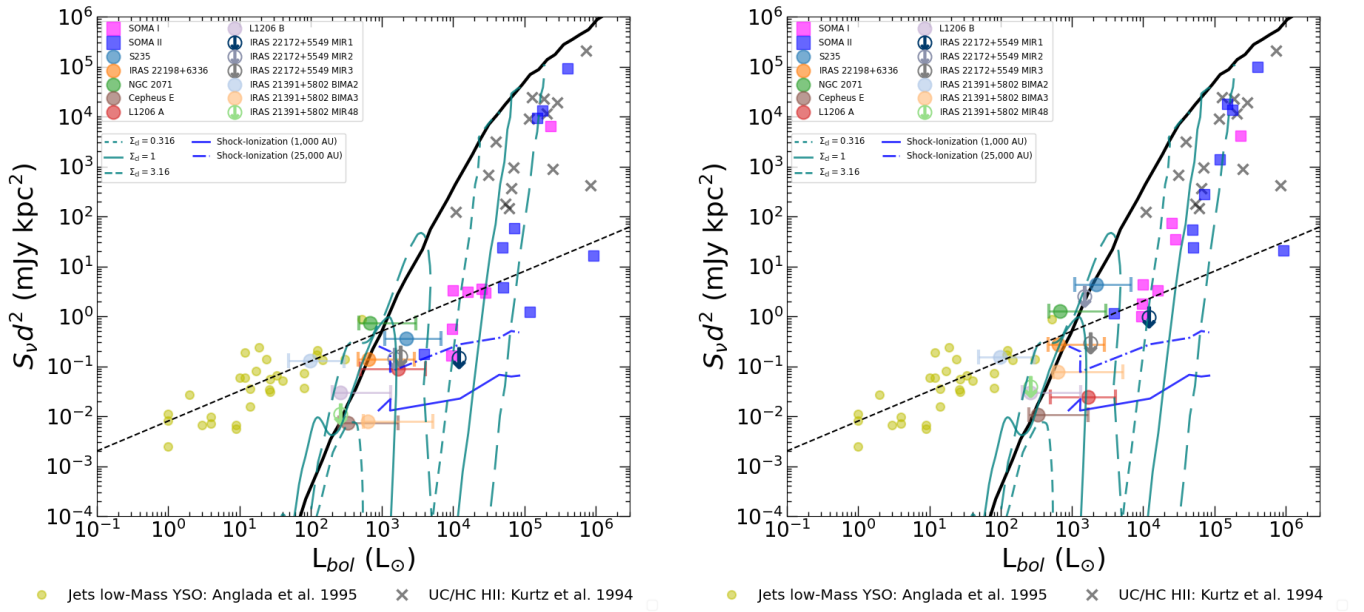


Figure A1. As Fig. 7, but now plotting $L_{\text{bol,iso}}$ for the SOMA sources (left: inner scale, right: SOMA scale).

B. EVOLUTIONARY TRACKS FROM RADIO LUMINOSITIES

Figure B1 makes a comparison of the SOMA Radio data at the inner (top) and SOMA (bottom) scale, with the full set of protostellar evolutionary tracks from Y. Zhang & J. C. Tan (2018), i.e., with $M_c = 10, 30, 60, 120, 240$ and $480 M_\odot$ with $\Sigma_{cl} = 0.316 \text{ g cm}^{-2}$ (left), 1 g cm^{-2} (center) and 3.16 g cm^{-2} (right). In these models the radio luminosities are not set from radiation transfer like the tracks from (K. E. I. Tanaka et al. 2016), but instead assumes a simple spherical HII region. Meanwhile, Figure B2 shows the same information but with the average of the good models of the isotropic bolometric luminosity (Table C.1 of SOMA V).

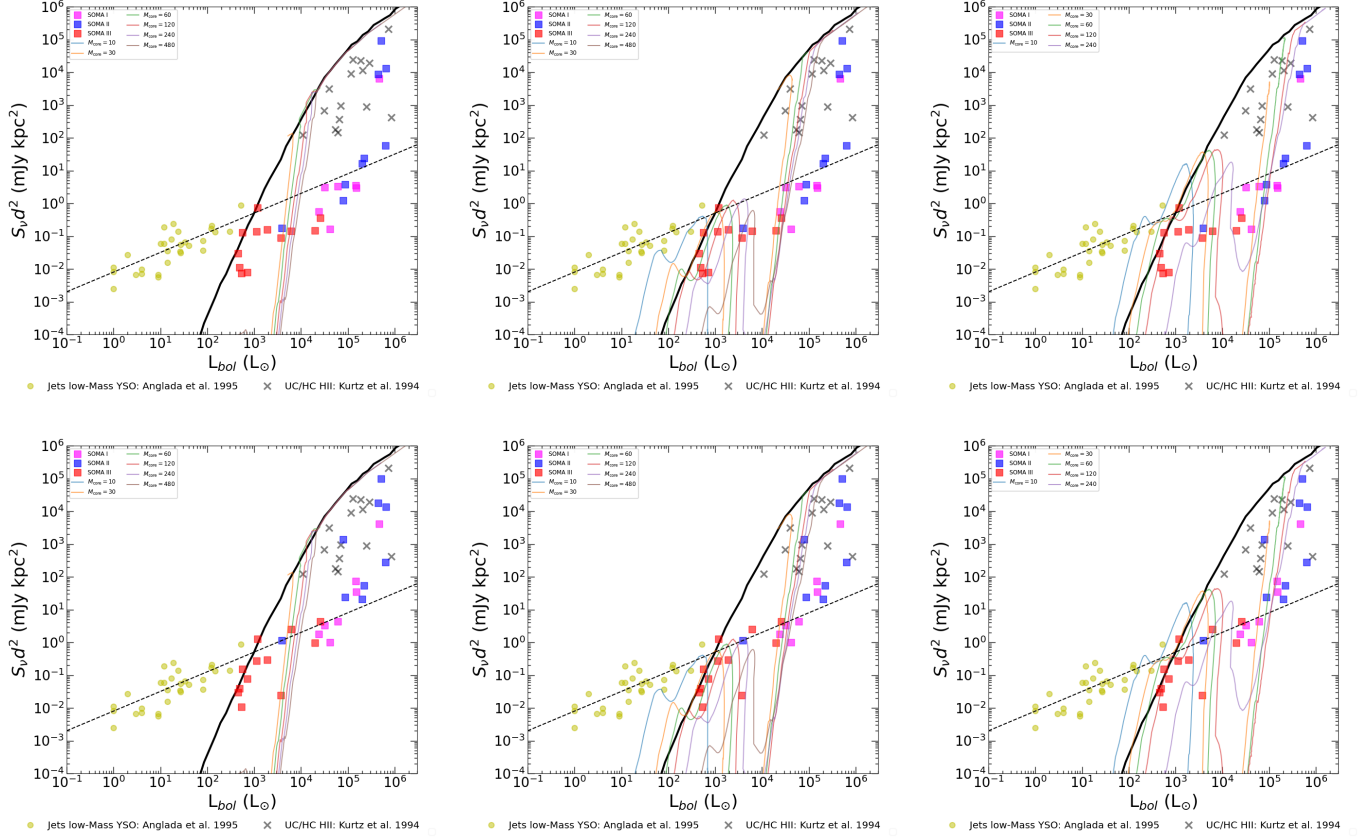


Figure B1. As Fig. 7, but now showing protostellar evolutionary tracks from Y. Zhang & J. C. Tan (2018), under the assumption of optically thin radio emission. These models are for $M_c = 10, 30, 60, 120, 240$ and $480 M_\odot$ with $\Sigma_{cl} = 0.316 \text{ g cm}^{-2}$ (left), 1 g cm^{-2} (center) and 3.16 g cm^{-2} (right). Top plots are with the radio luminosity at the inner scale and bottom plots are with the radio luminosity at the SOMA scale.

REFERENCES

- Anglada, G. 1995, in *Revista Mexicana de Astronomía y Astrofísica Conference Series*, Vol. 1, *Revista Mexicana de Astronomía y Astrofísica Conference Series*, ed. S. Lizano & J. M. Torrelles, 67
- Anglada, G., Rodríguez, L. F., & Carrasco-Gonzalez, C. 2015, in *Advancing Astrophysics with the Square Kilometre Array (AASKA14)*, 121, doi: [10.22323/1.215.0121](https://doi.org/10.22323/1.215.0121)
- Anglada, G., Villuendas, E., Estalella, R., et al. 1998, *AJ*, 116, 2953, doi: [10.1086/300637](https://doi.org/10.1086/300637)
- Astropy Collaboration, Robitaille, T. P., Tollerud, E. J., et al. 2013, *A&A*, 558, A33, doi: [10.1051/0004-6361/201322068](https://doi.org/10.1051/0004-6361/201322068)
- Astropy Collaboration, Price-Whelan, A. M., Sipőcz, B. M., et al. 2018, *AJ*, 156, 123, doi: [10.3847/1538-3881/aabc4f](https://doi.org/10.3847/1538-3881/aabc4f)
- Ayala, S., Noriega-Crespo, A., Garnavich, P. M., et al. 2000, *AJ*, 120, 909, doi: [10.1086/301500](https://doi.org/10.1086/301500)
- Bally, J. 1982, *ApJ*, 261, 558, doi: [10.1086/160366](https://doi.org/10.1086/160366)
- Bally, J., & Stark, A. A. 1983, *ApJL*, 266, L61, doi: [10.1086/183978](https://doi.org/10.1086/183978)
- Beltrán, M. T. 2015, *Ap&SS*, 355, 283, doi: [10.1007/s10509-014-2151-0](https://doi.org/10.1007/s10509-014-2151-0)
- Beltrán, M. T., Girart, J. M., & Estalella, R. 2006, *A&A*, 457, 865, doi: [10.1051/0004-6361:20065132](https://doi.org/10.1051/0004-6361:20065132)
- Beltrán, M. T., Girart, J. M., Estalella, R., Ho, P. T. P., & Palau, A. 2002, *ApJ*, 573, 246, doi: [10.1086/340592](https://doi.org/10.1086/340592)
- Boley, P. A., Sobolev, A. M., Krushinsky, V. V., et al. 2009, *MNRAS*, 399, 778, doi: [10.1111/j.1365-2966.2009.15308.x](https://doi.org/10.1111/j.1365-2966.2009.15308.x)
- Briggs, D. S. 1995, PhD thesis, New Mexico Institute of Mining and Technology
- Brogan, C. L., Hunter, T. R., Cyganowski, C. J., et al. 2016, *ApJ*, 832, 187, doi: [10.3847/0004-637X/832/2/187](https://doi.org/10.3847/0004-637X/832/2/187)
- Carrasco-González, C., Osorio, M., Anglada, G., et al. 2012, *ApJ*, 746, 71, doi: [10.1088/0004-637X/746/1/71](https://doi.org/10.1088/0004-637X/746/1/71)
- CASA Team, Bean, B., Bhatnagar, S., et al. 2022, *PASP*, 134, 114501, doi: [10.1088/1538-3873/ac9642](https://doi.org/10.1088/1538-3873/ac9642)

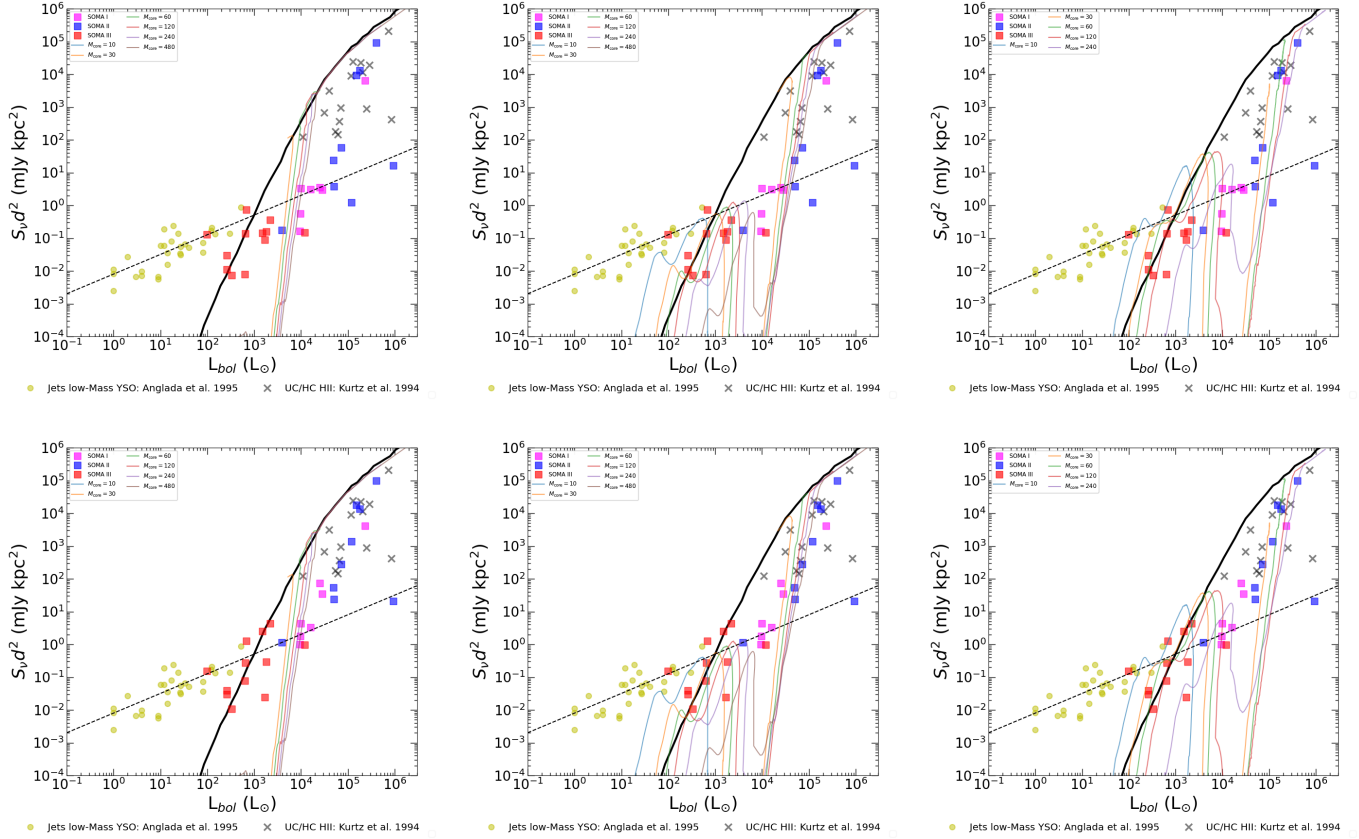


Figure B2. As Fig. B1, but now with the isotropic bolometric luminosity. Top plots are with the radio luminosity at the inner scale and bottom plots are with the radio luminosity at the SOMA scale.

Cheng, Y., Tobin, J. J., Yang, Y.-L., et al. 2022, *ApJ*, 933, 178, doi: [10.3847/1538-4357/ac7464](https://doi.org/10.3847/1538-4357/ac7464)

Choudhury, R., Mookerjee, B., & Bhatt, H. C. 2010, *ApJ*, 717, 1067, doi: [10.1088/0004-637X/717/2/1067](https://doi.org/10.1088/0004-637X/717/2/1067)

Codella, C., Bachiller, R., Nisini, B., Saraceno, P., & Testi, L. 2001, *A&A*, 376, 271, doi: [10.1051/0004-6361:20010963](https://doi.org/10.1051/0004-6361:20010963)

De Buizer, J. M., Liu, M., Tan, J. C., et al. 2017, *ApJ*, 843, 33, doi: [10.3847/1538-4357/aa74c8](https://doi.org/10.3847/1538-4357/aa74c8)

Dewangan, L. K., Ojha, D. K., Luna, A., et al. 2016, *ApJ*, 819, 66, doi: [10.3847/0004-637X/819/1/66](https://doi.org/10.3847/0004-637X/819/1/66)

Fedriani, R., Tan, J. C., Telkamp, Z., et al. 2023, *ApJ*, 942, 7, doi: [10.3847/1538-4357/aca4cf](https://doi.org/10.3847/1538-4357/aca4cf)

Felli, M., Massi, F., Robberto, M., & Cesaroni, R. 2006, *A&A*, 453, 911, doi: [10.1051/0004-6361:20054646](https://doi.org/10.1051/0004-6361:20054646)

Fontani, F., Cesaroni, R., Testi, L., et al. 2004, *A&A*, 424, 179, doi: [10.1051/0004-6361:20035848](https://doi.org/10.1051/0004-6361:20035848)

Garay, G., Mardones, D., & Rodríguez, L. F. 2000, *ApJ*, 545, 861, doi: [10.1086/317853](https://doi.org/10.1086/317853)

Gardiner, E. C., Tan, J. C., Staff, J. E., et al. 2024, *ApJ*, 967, 145, doi: [10.3847/1538-4357/ad39e1](https://doi.org/10.3847/1538-4357/ad39e1)

Gusdorf, A., Anderl, S., Lefloch, B., et al. 2017, *A&A*, 602, A8, doi: [10.1051/0004-6361/201730454](https://doi.org/10.1051/0004-6361/201730454)

Herbig, G. H. 1960, *ApJS*, 4, 337, doi: [10.1086/190050](https://doi.org/10.1086/190050)

Heyer, M. H., Carpenter, J. M., & Ladd, E. F. 1996, *ApJ*, 463, 630, doi: [10.1086/177277](https://doi.org/10.1086/177277)

Hirota, T., Ando, K., Bushimata, T., et al. 2008, *PASJ*, 60, 961, doi: [10.1093/pasj/60.5.961](https://doi.org/10.1093/pasj/60.5.961)

Jenness, T., Scott, P. F., & Padman, R. 1995, *MNRAS*, 276, 1024, doi: [10.1093/mnras/276.3.1024](https://doi.org/10.1093/mnras/276.3.1024)

Kavak, Ü., Sánchez-Monge, Á., López-Sepulcre, A., et al. 2021, *A&A*, 645, A29, doi: [10.1051/0004-6361/202037652](https://doi.org/10.1051/0004-6361/202037652)

Kurtz, S., Churchwell, E., & Wood, D. O. S. 1994, *ApJS*, 91, 659, doi: [10.1086/191952](https://doi.org/10.1086/191952)

Lefloch, B., Cernicharo, J., Pacheco, S., & Ceccarelli, C. 2011, *A&A*, 527, L3, doi: [10.1051/0004-6361/201016247](https://doi.org/10.1051/0004-6361/201016247)

Lefloch, B., Eisloffel, J., & Lazareff, B. 1996, *A&A*, 313, L17

Lefloch, B., Gusdorf, A., Codella, C., et al. 2015, *A&A*, 581, A4, doi: [10.1051/0004-6361/201425521](https://doi.org/10.1051/0004-6361/201425521)

Liu, D.-J., Xu, Y., Li, Y.-J., et al. 2021, *ApJS*, 253, 15, doi: [10.3847/1538-4365/abcece](https://doi.org/10.3847/1538-4365/abcece)

Liu, M., Tan, J. C., De Buizer, J. M., et al. 2019, *ApJ*, 874, 16, doi: [10.3847/1538-4357/ab07b7](https://doi.org/10.3847/1538-4357/ab07b7)

- Liu, M., Tan, J. C., De Buizer, J. M., et al. 2020, *ApJ*, 904, 75, doi: [10.3847/1538-4357/abbefb](https://doi.org/10.3847/1538-4357/abbefb)
- Matthews, H. I. 1979, *A&A*, 75, 345
- McMullin, J. P., Waters, B., Schiebel, D., Young, W., & Golap, K. 2007, in *Astronomical Society of the Pacific Conference Series*, Vol. 376, *Astronomical Data Analysis Software and Systems XVI*, ed. R. A. Shaw, F. Hill, & D. J. Bell, 127
- Molinari, S., Testi, L., Rodríguez, L. F., & Zhang, Q. 2002, *ApJ*, 570, 758, doi: [10.1086/339630](https://doi.org/10.1086/339630)
- Moro-Martín, A., Noriega-Crespo, A., Molinari, S., et al. 2001, *ApJ*, 555, 146, doi: [10.1086/321443](https://doi.org/10.1086/321443)
- Nakano, M., & Yoshida, S. 1986, *PASJ*, 38, 531
- Neri, R., Fuente, A., Ceccarelli, C., et al. 2007, *A&A*, 468, L33, doi: [10.1051/0004-6361:20077320](https://doi.org/10.1051/0004-6361:20077320)
- Ospina-Zamudio, J., Lefloch, B., Ceccarelli, C., et al. 2018, *A&A*, 618, A145, doi: [10.1051/0004-6361/201832857](https://doi.org/10.1051/0004-6361/201832857)
- Ospina-Zamudio, J., Lefloch, B., Favre, C., et al. 2019, *MNRAS*, 490, 2679, doi: [10.1093/mnras/stz2733](https://doi.org/10.1093/mnras/stz2733)
- Palau, A., Fuente, A., Girart, J. M., et al. 2013, *ApJ*, 762, 120, doi: [10.1088/0004-637X/762/2/120](https://doi.org/10.1088/0004-637X/762/2/120)
- Panagia, N. 1973, *AJ*, 78, 929, doi: [10.1086/111498](https://doi.org/10.1086/111498)
- Panagia, N., & Walmsley, C. M. 1978, *Astronomy and Astrophysics*, 70, 411
- Pecaut, M. J., & Mamajek, E. E. 2013, *ApJS*, 208, 9, doi: [10.1088/0067-0049/208/1/9](https://doi.org/10.1088/0067-0049/208/1/9)
- Purser, S. J. D., Lumsden, S. L., Hoare, M. G., & Kurtz, S. 2021, *MNRAS*, 504, 338, doi: [10.1093/mnras/stab747](https://doi.org/10.1093/mnras/stab747)
- Ressler, M. E., & Shure, M. 1991, *AJ*, 102, 1398, doi: [10.1086/115965](https://doi.org/10.1086/115965)
- Reynolds, S. P. 1986, *ApJ*, 304, 713, doi: [10.1086/164209](https://doi.org/10.1086/164209)
- Robitaille, T. 2019, *APLpy v2.0: The Astronomical Plotting Library in Python*, doi: [10.5281/zenodo.2567476](https://doi.org/10.5281/zenodo.2567476)
- Robitaille, T., & Bressert, E. 2012, *APLpy: Astronomical Plotting Library in Python*, *Astrophysics Source Code Library* <http://ascl.net/1208.017>
- Rosero, V., Tanaka, K. E. I., Tan, J. C., et al. 2019a, *ApJ*, 873, 20, doi: [10.3847/1538-4357/ab0209](https://doi.org/10.3847/1538-4357/ab0209)
- Rosero, V., Hofner, P., Claussen, M., et al. 2016, *ApJS*, 227, 25, doi: [10.3847/1538-4365/227/2/25](https://doi.org/10.3847/1538-4365/227/2/25)
- Rosero, V., Hofner, P., Kurtz, S., et al. 2019b, *ApJ*, 880, 99, doi: [10.3847/1538-4357/ab2595](https://doi.org/10.3847/1538-4357/ab2595)
- Ruiz, A., Rodríguez, L. F., Canto, J., & Mirabel, I. F. 1992, *ApJ*, 398, 139, doi: [10.1086/171843](https://doi.org/10.1086/171843)
- Rygl, K. L. J., Brunthaler, A., Reid, M. J., et al. 2010, *A&A*, 511, A2, doi: [10.1051/0004-6361/200913135](https://doi.org/10.1051/0004-6361/200913135)
- Sánchez-Monge, Á., Palau, A., Estalella, R., Beltrán, M. T., & Girart, J. M. 2008, *A&A*, 485, 497, doi: [10.1051/0004-6361:20078406](https://doi.org/10.1051/0004-6361:20078406)
- Sánchez-Monge, Á., Palau, A., Estalella, R., et al. 2010, *ApJL*, 721, L107, doi: [10.1088/2041-8205/721/2/L107](https://doi.org/10.1088/2041-8205/721/2/L107)
- Sargent, A. I. 1977, *ApJ*, 218, 736, doi: [10.1086/155729](https://doi.org/10.1086/155729)
- Sequeira-Murillo, F., Rosero, V., Marvil, J., et al. 2025, *arXiv e-prints*, arXiv:2507.16775, doi: [10.48550/arXiv.2507.16775](https://doi.org/10.48550/arXiv.2507.16775)
- Sugitani, K., Matsuo, H., Nakano, M., Tamura, M., & Ogura, K. 2000, *AJ*, 119, 323, doi: [10.1086/301164](https://doi.org/10.1086/301164)
- Surcis, G., Vlemmings, W. H. T., van Langevelde, H. J., Hutawarakorn Kramer, B., & Quiroga-Núñez, L. H. 2013, *A&A*, 556, A73, doi: [10.1051/0004-6361/201321501](https://doi.org/10.1051/0004-6361/201321501)
- Tanaka, K. E. I., Tan, J. C., & Zhang, Y. 2016, *ApJ*, 818, 52, doi: [10.3847/0004-637X/818/1/52](https://doi.org/10.3847/0004-637X/818/1/52)
- Telkamp, Z., Fedriani, R., Tan, J. C., et al. 2025, *The Astrophysical Journal*, 986, 15, doi: [10.3847/1538-4357/adcd79](https://doi.org/10.3847/1538-4357/adcd79)
- Thompson, R. I. 1984, *ApJ*, 283, 165, doi: [10.1086/162287](https://doi.org/10.1086/162287)
- Tobin, J. J., Sheehan, P. D., Megeath, S. T., et al. 2020, *ApJ*, 890, 130, doi: [10.3847/1538-4357/ab6f64](https://doi.org/10.3847/1538-4357/ab6f64)
- Torrelles, J. M., Gómez, J. F., Rodríguez, L. F., et al. 1998, *ApJ*, 505, 756, doi: [10.1086/306205](https://doi.org/10.1086/306205)
- Trinidad, M. A., Rodríguez, T., & Rodríguez, L. F. 2009, *ApJ*, 706, 244, doi: [10.1088/0004-637X/706/1/244](https://doi.org/10.1088/0004-637X/706/1/244)
- Valdettaro, R., Palla, F., Brand, J., & Cesaroni, R. 2005, *A&A*, 443, 535, doi: [10.1051/0004-6361:20053731](https://doi.org/10.1051/0004-6361:20053731)
- Willing, B., Mundy, L., McMullin, J., Hezel, T., & Keene, J. 1993, *AJ*, 106, 250, doi: [10.1086/116633](https://doi.org/10.1086/116633)
- Zhang, Y., & Tan, J. C. 2018, *ApJ*, 853, 18, doi: [10.3847/1538-4357/aaa24a](https://doi.org/10.3847/1538-4357/aaa24a)